공학박사 학위논문

# Electrochemical Evaluation of Titanium Oxide and Tin Oxide as High Power Anode Materials for Lithium-Ion Batteries

리튬 이온 전지 고출력 음극 물질로서

이산화티타늄과 이산화주석의 전기화학적 평가

2015 년 2 월

서울대학교 대학원

화학생물공학부

엄 지 현

# Electrochemical Evaluation of Titanium Oxide and Tin Oxide as High Power Anode Materials for Lithium-Ion Batteries

지도교수 성 영 은

이 논문을 공학박사 학위논문으로 제출함
2015 년 2 월

서울대학교 대학원
화학생물공학부
엄 지 현

엄지현의 공학박사 학위논문을 인준함
2015 년 2 월

위 원 장 _____ (인)

부위원장 _____ (인)

위 원 _____ (인)

위 원 _____ (인)

위 원 _____ (인)

## Abstract

# Electrochemical Evaluation of Titanium Oxide and Tin Oxide as High Power Anode Materials for Lithium-Ion Batteries

JiHyun Um

School of Chemical & Biological Engineering

Seoul National University

The development of electric vehicles (EVs) has been stimulated with the advent of the era of clean energy, leading to the commercialization of hybrid electric vehicles (HEVs), powered by an internal combustion engine and an electric motor that utilizes energy stored in lithium-ion batteries (LIBs), and the rapid development of battery electric vehicles (BEVs) using only battery as a power source. The demand for power performance in the battery of EVs is more than 50 times higher than in the small electric devices such as cellular phones and laptop computers. The high power performance is

associated with the various factors including electrode material, electrode structure, ion conductivity of electrolyte, etc. For the anode materials at present known, energy density (Watt-hours) and power density (Watt) are trade-off relation, which expedites the following researches for the realization of high power performance from high energy density materials: (1) new material development (2) electrode filming (3) design of integrated electrode (4) understanding of reaction mechanism and design for new electrode material using ab initio quantum chemistry methods. In this dissertation, high power density through the material design and the integrated electrode architecture utilizing the character of thin film electrode potentially will be discussed.

Chapter 1 begins with general overview of LIBs and materials of cathode and anode categorized according to structure and reaction mechanism, respectively. In addition, titanium oxide known as a typical anode material with high rate capability and tin oxide having a high theoretical capacity in anode materials are introduced.

Chapter 2 describes the electrochemical properties of titanium oxide. In particular, the effect of particle size controlled with three different size groups on the power density is discussed. The structural changes upon cycling were analyzed by *in-situ* synchrotron X-ray diffraction. The increase of capacity upon cycling like activation was observed in all size groups, which is rarely reported in the stable anode material following intercalation reaction mechanism. As a reason for this phenomena, I propose the enhancement of contact area between active material and electrolyte resulted from lattice expansion upon

cycling through *in-situ* synchrotron X-ray diffraction analysis.

Chapter 3 introduces an approach to improve the electrochemical performance of tin oxide. Compared with conventional LIBs electrode in 2-dimensional (2D) laminate structure, electrode design was extended into 3-dimensional (3D) architecture of copper foam applied to template for the deposition of tin oxide. The copper foam, served as a current collector and a template for forming a thin layer of tin oxide, is advantageous for alleviating the large volume changes of tin oxide during cycling by providing void space. The integrated electrode is free of binder and conducting agent, exhibiting a high reversible capacity, good rate capability, and stable cycle retention with maintaining a structural integrity. As another electrode architecture, copper layer-by-layer assembly is introduced. Many pores are developed on the surface of each layer, penetrating the layer and creating an open pore system. Consequently, the copper layer-by-layer assembly with high surface area realizes excellent power performance even at very high current densities from tin oxide of high capacity anode material.

**Keywords:** Lithium-ion battery, Electrode architecture, High power density, Titanium oxide, Tin oxide

**Student Number:** 2011-30279

# Contents

# List of Tables

## Chapter 1



## Chapter 2



## Chapter 3

# List of Figures

## Chapter 1



## Chapter 2

## Chapter 3

# Chapter 1. Introduction

## 1.1 Lithium-ion batteries

### 1.1.1. General introduction

Beyond the extensive usage of portable electronics and development of electric vehicles at present, electrical energy storage from alternative energy sources is demanded in future, which emphasizes the role of energy storage[1]. Among the numerous energy storage technologies, lithium-ion batteries (LIBs) have received attention because of their high gravimetric and volumetric energy densities (Fig. 1.1)[1,2].

LIBs consist of cathode, anode, electrolyte, and separator as illustrated in Fig. 1.2. Two electrodes (cathode and anode) are separated by separator filled with organic electrolyte. When an electrical load is applied to the cell, Li ion is extracted from anode, passing through the organic electrolyte that easily conducts Li ions and the polymer separator with insulating properties, and is inserted to cathode[3-5]. Electron is transferred simultaneously from anode to cathode through an external circuit. These reactions are reversible during charging process. The overall insertion/extraction of Li ion can be expressed by the following reactions[6,7]:

$$LiCoO_2 \leftrightarrow 0.5Li^+ + 0.5e^- + Li_{0.5}CoO_2 \quad \text{(cathode)}$$

$$C_6 + Li^+ + e^- \leftrightarrow LiC_6 \quad \text{(anode)}$$

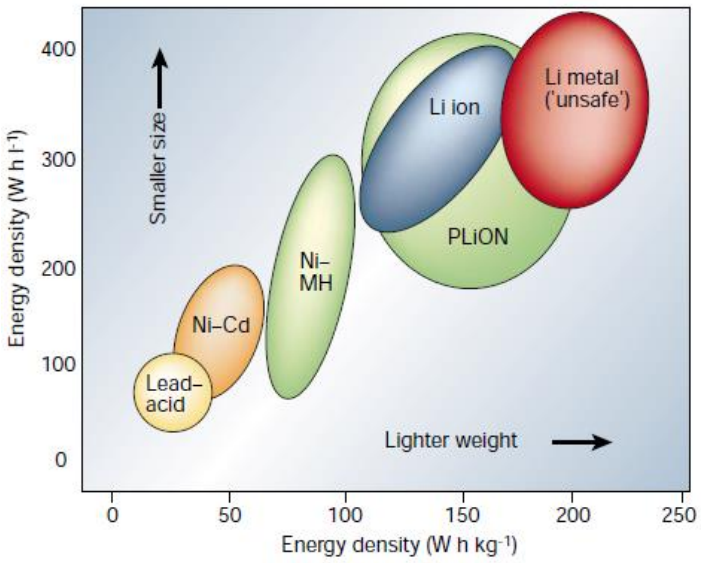


**Fig. 1.1** Comparison of the different battery technologies in terms of volumetric and gravimetric energy density.

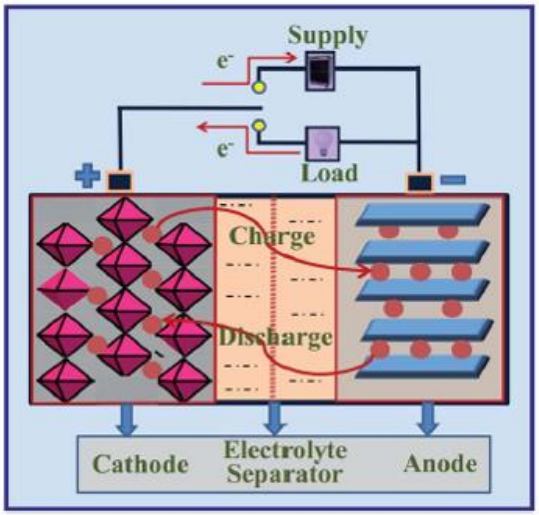


**Fig. 1.2** Schematic illustration of lithium-ion battery.

The choice of the electrode materials impacts on the operating voltage, capacity, life time, and safety of the LIBs[8,9]. Also, optimization condition is dependent on the choice of electrode materials in full cell battery system. The gravimetric and volumetric capacities of the active materials reacting with Li ion are illustrated in Fig. 1.3. The common concept of the currently used LIBs relies on transition metals oxides or phosphates material such as $LiCoO_2$, $LiMn_2O_4$, $LiCo_{1/3}Mn_{1/3}Ni_{1/3}O_2$, $LiFePO_4$ in cathode, while graphite is commonly applied to anode material.

The cathode materials can be classified into the three types of metal oxides with layered structure, spinel structure, olivine structures as shown in Fig. 1.4. Since $LiCoO_2$ was used as cathode material of the newly invented LIBs (1980), most of the commercially available LIBs are still using cathode materials based on $LiCoO_2$ from 2006, while various researches have been done for developing a new cathode material with higher energy density, lower cost than $LiCoO_2$, and more safety. Milestones were made for the $LiCoO_2$ layered structure in 1980[10], the $LiMn_2O_4$ spinels in 1986[11,12], and the Li*M*$PO_4$ (*M* = Mn, Fe, etc.) olivine group in 1997[13]. Table 1.1 summarizes the operating voltage and capacity of the compound with three structure types. Layered structured materials are used as cathode for high energy density systems[14,15], while spinel structured and olivine structured materials are candidate in the case of high power density systems[16,17].

The three main groups of reaction mechanism for anode materials in Fig. 1.5.

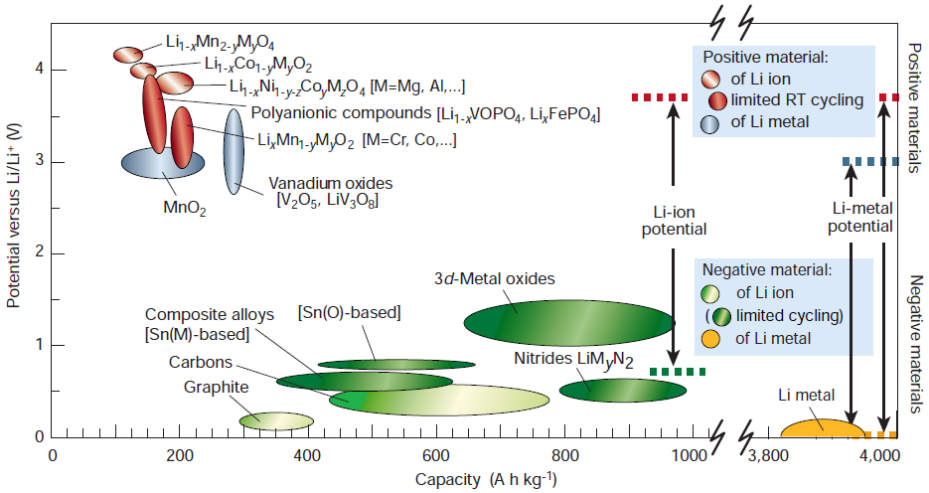


**Fig. 1.3** Voltage versus capacity for positive- and negative-electrode materials presently used or under serious considerations for the next generation of rechargeable Li-based cells.

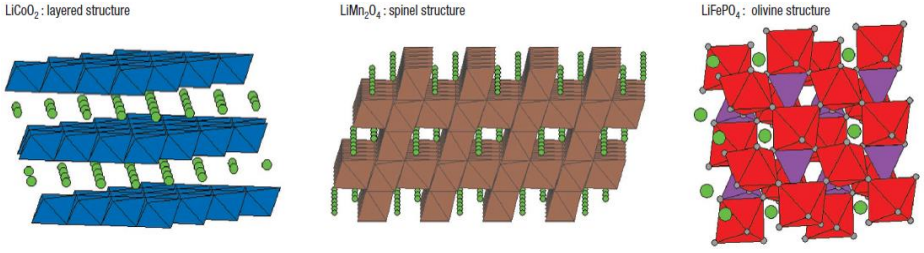


**Fig. 1.4** Schematic crystal structures of three types of cathode materials.

**Table 1.1** Electrochemical characteristics of the three classes of insertion compounds.

| Framework | Compound | Specific capacity [a] ($mAh\ g^{-1}$) | Average potential (V *vs.* $Li^0/Li^+$) |
|---|---|---|---|
| Layered | $LiCoO_2$ | 272 (140) | 4.2 |
| | $LiNi_{1/3}Mn_{1/3}Co_{1/3}O_2$ | 272 (200) | 4.0 |
| Spinel | $LiMn_2O_4$ | 148 (120) | 4.1 |
| | $LiMn_{3/2}Ni_{1/2}O_4$ | 148 (120) | 4.7 |
| Olivine | $LiFePO_4$ | 170 (160) | 3.45 |
| | $LiFe_{1/2}Mn_{1/2}PO_4$ | 170 (160) | 3.4/4.1 |

1) Intercalation/de-intercalation reaction materials: carbon based materials such as graphite, porous carbon, graphene, $Li_4Ti_5O_{12}$, $TiO_2$, etc.
2) Conversion reaction materials: Transition metal oxides ($Fe_xO_y$, NiO, CuO, $Cu_2O$, $Mn_xO_y$, $MoO_2$), metal nitrides, metal phosphides, and metal sulphides, etc.
3) Alloy/de-alloy reaction materials: Si, Ge, Sn, $SnO_2$, Pb, Al, Bi, etc.

Graphite and $Li_4Ti_5O_{12}$ are well known as intercalation/de-intercalation reaction materials. The volume changes with full Li ion intercalation in graphite ($LiC_6$) is less than 9%, indicating a good cyclic stability[18-21]. In particular, $Li_4Ti_5O_{12}$ is regarded as a zero strain material during repeated charge and discharge process. In spite of their high intercalation and de-intercalation reversibility, graphite and $Li_4Ti_5O_{12}$ is limited to their low theoretical capacity of 372 mAh $g^{-1}$ and 175 mAh $g^{-1}$, respectively[22-24]. Conversion materials such as $M_xN_y$ (M = Co, Fe, Mn, Cu, Ni and N = O, N, P, and S) involve Li ion in their compound, which indicates that the reduction (oxidation) of transition metal accompanying with the composition (decomposition) of the compounds for $Li_xN_y$ (N = O, N, P, and S). Since a high number of electrons participate in the conversion reactions, these compounds delivers high reversible capacities as shown in Fig. 1.6. However, the application of conversion materials have been hindered by the inherently severe volume expansion and contraction during the large amounts of Li ion insertion and extraction, which can cause a pulverization of active material and a loss of electrical contact, and eventually resulting in poor capacity retention[6,25].

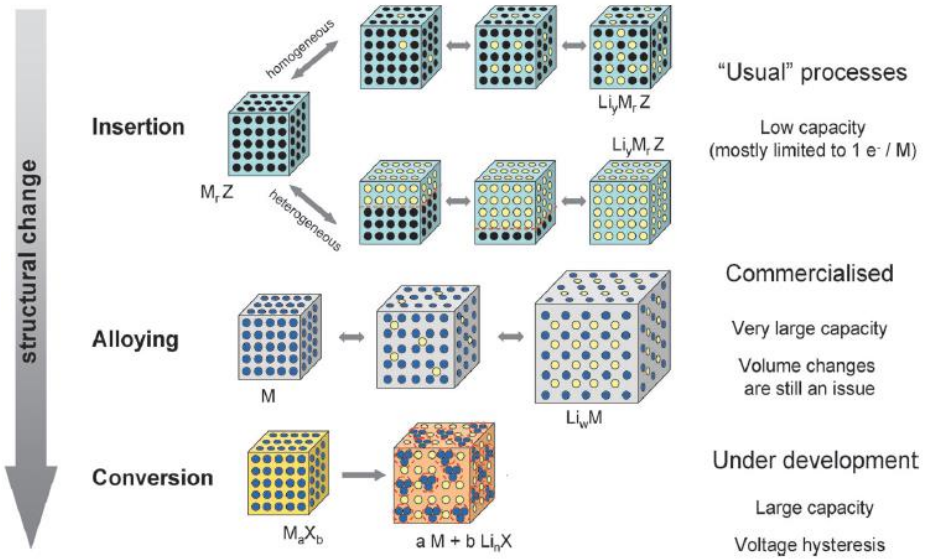


**Fig. 1.5** Schematic representation of different anode reaction mechanisms.

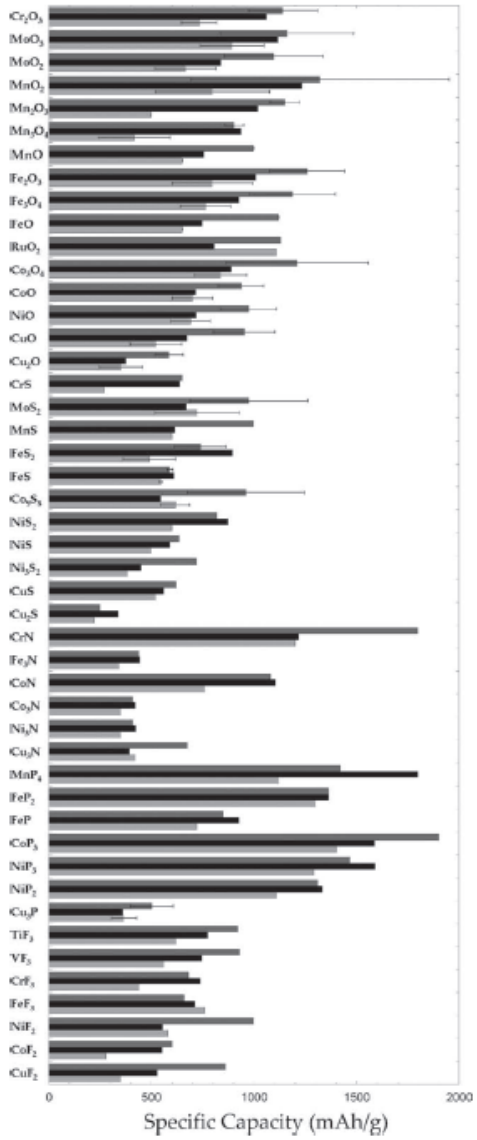


**Fig. 1.6** Theoretical (black bar), first discharge (dark grey), and charge (light grey) specific capacities of different compounds following conversion reaction.

Alloy/de-alloy materials, Si, Ge, Sn, $SnO_2$, Pb, Al, Bi, have high capacity in general, especially for Si with a theoretical capacity of 4200 mAh $g^{-1}$. Also in the same manner, the alloy/de-alloy materials such as $Li_{22}Si_5$ and $Li_{17}M_4$ (M = Ge, Sn, and Pb) involving the high number of Li ions undergo the large volume changes causing the pulverization of active material and the electrical contact loss with current collector[26-28].

### 1.1.2. Titanium oxide

Titanium oxide has been one of the most useful material in various fields especially in energy applications such as photo-catalysts, solar cells, and Li ion batteries (LIBs)[2,4]. Among these, titanium oxide nanoparticles as the anode material for LIBs have very attractive characteristics of good cycling life, rapid discharge/charge rate, safety, etc[29,30]. The insertion/extraction of Li ion into/from the $TiO_2$ can be expressed as the reversible intercalation reactions according to the following reaction:

$$TiO_2 + xLi^+ + xe^- \leftrightarrow Li_xTiO_2$$

For titanium oxide ($TiO_2$), four polymorphs are well known as a Li ion intercalation host in Fig. 1.7: anatase (space group *I*41/*amd*), rutile (*P*42/*mnm*), brookite (*Pbca*), and $TiO_2$ B ("bronze", *C*2/*m*). $TiO_2$ with relative high operation voltage is free from the formation of solid-electrolyte interface (SEI) layer over that of most anode materials such as graphite, Si, and Sn (below 0.5 V)[31], which makes batteries unstable and unsafe. Good stability or long lasting cycling property of $TiO_2$ are thanks to the small volume changes (less than 4%) during insertion/extraction of Li ion because stability problems is usually comes from large volume expansion and contraction of active materials like Si, Sn, etc[32]. These properties are gaining more and more importance in the present needs of emerging automobile such as hybrid or full electric vehicles (EVs) because of more advantages over the conventional anode materials for accomplishing higher stability and safety[7,33].

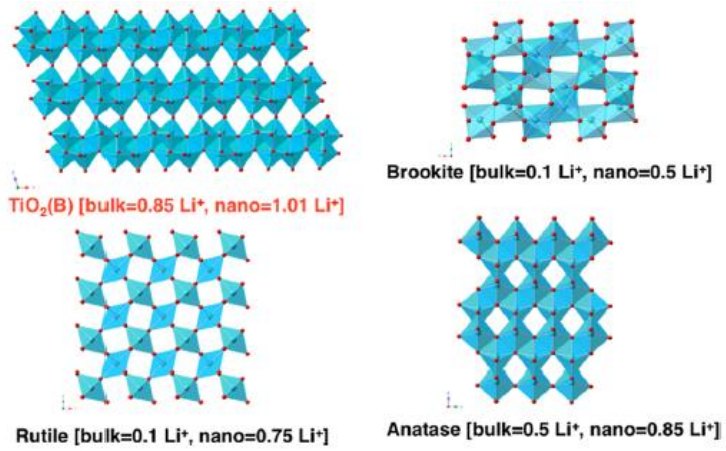


**Fig. 1.7** Four polymorphs of titanium oxide.

### 1.1.3. Tin oxide

By growing demand in various applications of LIBs, development of high-performance materials with higher energy and power density and better cycling stability has been stimulated,[4,23] leading to the significant progress in high capacity anode materials such as Sn and Si compared to commercially used graphite limited by a theoretical capacity of 372 mAh $g^{-1}$. However, the practical application of these high capacity materials is impeded by poor capacity retention resulting from inherently large volume changes (up to 300% and 400% for Sn and Si, respectively) during Li ion insertion and extraction.[3,16] Substantial efforts are devoted to relieve the large volume changes causing pulverization of active material and electrical contact loss with the current collector: reducing the particle size to the nanoscale,[7,34] hybridizing with carbon or polymers,[35] and controlling dimensions for unique architectures.[11,36]

One-dimensional (1D) nanostructures have fascinating advantages compared to their bulk counterparts, and demonstrate their improved performance such as Si,[5] $SnO_2$,[12] $Co_3O_4$,[37] $Fe_2O_3$,[16] and $TiO_2$[27] anodes. In particular, nanotubes grown directly on current collector substrate are expected to having the following advantages.[18-20] First, since each nanotube is connected to the current collector, every nanotube contributes to the capacity, and also binder or conductive additives are not required. Second, the tubular structure has a large interior void space to accommodate the volume change stresses. Third, the open end and thin wall structures allow for more efficient Li ion diffusion at exterior and

interior surfaces, which enables more symmetric volume changes and larger charge storage. Furthermore, direct channels for efficient electron pathways enhance charge transport. Among the various synthetic strategies to prepare the nanotubes, template-assisted approach is widely explored and demonstrated to be an excellent method including nanofibers,[21] CNTs,[4] composite nanowires,[3] anodic aluminum oxide (AAO),[23] and polycarbonate (PC) membrane[28] template.

Two-dimensional (2D) structures with layered crystalline structures**,** **s**imilar to the structure of graphite**,** have attracted much interest as Li ion storage materials in recent years since the crystallographic transformation of layered materials can alleviate the volume changes during repeated discharge/charge process and provide the sufficient active sites for accommodation of Li ion[13]. In particular, the integration of nanosized current collector with metal oxides offers attractive opportunities for ultrafast power densities. The general details are illustrated in Fig. 1.8.

Three-dimensional (3D) interpenetrating network was regarded as the ideal electrode architecture to provide efficient Li ion and electron pathways by Long and Rolison[18] and also demonstrated to surpass traditional planar architecture at intermediate and high rates through simulations[19]. Currently, the 3D scaffold architecture has attracted attention as a smart electrode prototype, and various researches about the 3D network architecture from simple periodic sets of cylindrical electrodes[38] to complex arrangements such as foams or long chains of particles have been explored[18,32].

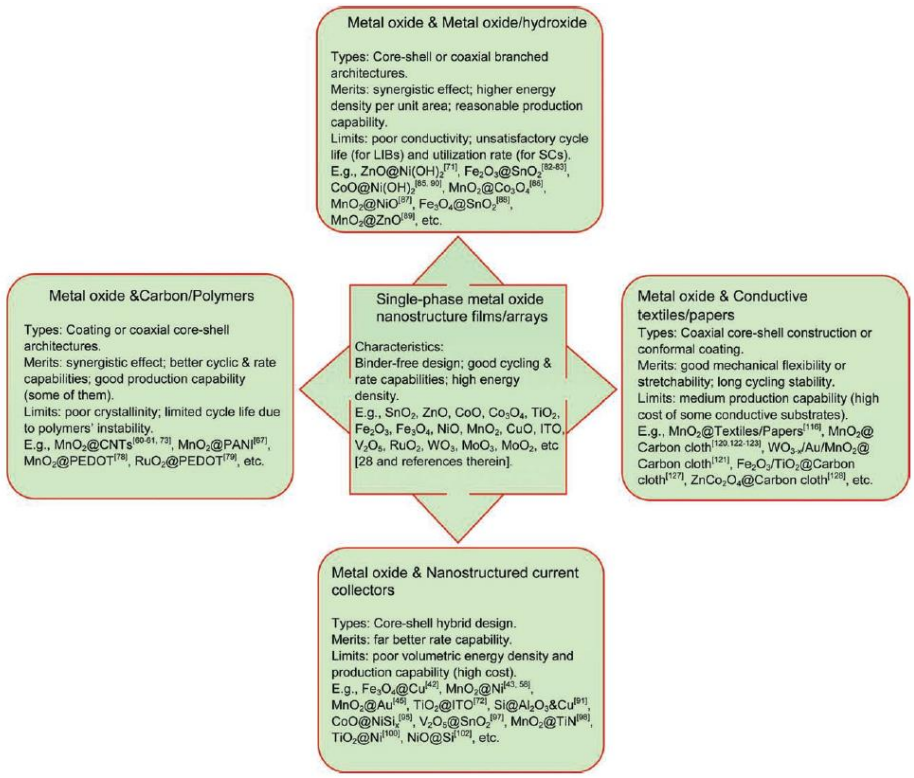


**Fig. 1.8** Four typical hybrid systems of metal oxide-based nanostructure.

## 1.2 References


1. Y. Idota, T. Kubota, A. Matsufuji, Y. Maekawa and T. Miyasaka, *Science*, 1997, **276**, 1395.

2. I. A. Courtney and J. R. Dahn, *J. Electrochem. Soc.*, 1997, **144**, 2045.

3. H. Tong, Y.-J. Zhu, L.-X. Yang, L. Li and L. Zhang, *Angew. Chem. Int. Ed.*, 2006, **45**, 7739.

4. N. Du, H. Zhang, B. Chen, X. Ma, Z. Liu, J. Wu and D. Yang, *Adv. Mater.*, 2007, **19**, 1641.

5. M. R. Zamfir, H. T. Nguyen, E. Moyen, Y. H. Lee and D. Pribat, *J. Mater. Chem. A*, 2013, **1**, 9566.

6. G. Cui, Y.-S. Hu, L. Zhi, D. Wu, I. Lieberwirth, J. Maier and K. Müllen, *Small*, 2007, **3**, 2066.

7. J. R. Dahn, T. Zheng, Y. Liu and J. S. Xue, *Science*, 1995, **270**, 590.

8. R. Mukherjee, A. V. Thomas, A. Krishnamurthy and N. Koratkar, *ACS Nano*, 2012, **6**, 7867.

9. J. Liu, Y. Li, X. Huang, R. Ding, Y. Hu, J. Jiang and L. Liao, *J. Mater. Chem.*, 2009, **19**, 1859.

10. K. Mizushima, P.C. Jones, P. J. Wiseman and J. B. Goodenough, *Mater. Res. Bull.*, 1980, **15**, 783.

11. M. M. Thackeray, W. I. F. David, P. G. Bruce and J. B. Goodenough, *Mater. Res. Bull.*, 1983, **18**, 461.

12. P. Meduri, C. Pendyala, V. Kumar, G. U. Sumanasekera and M. K. Sunkara, *Nano Lett.*, 2009, **9**, 612.

13. A. K. Padhi, K. S. Nanjundaswamy and J. B. Goodenough, *J. Electrochem. Soc.*, 1997, **144**, 1188.

14. J. P. Peres, F. Weill and C. Delmas, *Solid State Ion.*, 1999, **116**, 19.

15. T. Ohzuku and Y. Makimura, *Chem. Lett.*, 2001, **30**, 642.

16. N. Du, Y. Xu, H. Zhang, C. Zhai and D. Yang, *Nanoscale Res Lett.*, 2010, **5**, 1295.

17. K. Zaghib, A. Mauger, H. Groult, J. B. Goodenough and C. M. Julien, *Materials*, 2013, **6**, 1028.

18. H. Zhang, X. Yu, P. V. Braun, *Nat. Nanotechnol.*, 2011, **6**, 277.

19. R. Ed. Garcíaa and Y.-M. Chiang, *J. Electrochem. Soc.*, 2007, **154**, A856.

20. Y. Fu, Z. Yang, X. Li, X. Wang, D. Liu, D. Hu, L. Qiao and D. He, *J. Mater. Chem. A*, 2013, **1**, 10002.

21. J.-Y. Gong, S.-R. Guo, H.-S. Qian, W.-H. Xu and S.-H. Yu, *J. Mater. Chem.*, 2009, **19**, 1037.

22. J. Lin, Z. Peng, C. Xiang, G. Ruan, Z. Yan, D. Natelson and J. M. Tour, *ACS Nano*, 2013, **7**, 6001.

23. Z. Favors, W. Wang, H. H. Bay, A. George, M. Ozkan and C. S. Ozkan, *Sci. Rep.*, 2014, **4**, 4605.

24. J. Y. Xiang, J. P. Tu, Y. F. Yuan, X. H. Huang, Y. Zhou and L. Zhang, *Electrochem. Commun.*, 2009, **11**, 262.

25. M. Bhagwat, P. Shah and V. Ramaswamy, *Mater. Lett.*, 2003, **57**, 1604.

26. Y.-Y. Zhu, S.-R. Wang, L.-J. Zhu, X.-L. Ge, X.-B. Li and Z.-Y. Luo, *Catal. Lett.*, 2010, **135**, 275.

27. J. Wu, S. Lo, K. Song, B. K. Vijayan, W. Li, K. A. Gray and V. P. Dravid, *J. Mater. Res.*, 2011, **26**, 1646.

28. N. Li, C. R. Martin and B. Scrosati, *Electrochem. Solid-State Lett.*, 2000, **3**, 316.

29. Y. Yang, X. Ji, F. Lu, Q. Chena and C. E. Banks, *Phys. Chem. Chem. Phys.*, 2013, **15**, 15098.

30. K. Kravchyk, L. Protesescu, M. I. Bodnarchuk, F. Krumeich, M. Yarema, M. Walter, C. Guntlin and M. V. Kovalenko, *J. Am. Chem. Soc.*, 2013, **135**, 4199.

31. R. Demir-Cakan, Y.-S. Hu, M. Antonietti, J. Maier and M.-M. Titirici, *Chem. Mater.*, 2008, **20**, 1227.

32. Y. Yu, L. Gu, C. Wang, A. Dhanabalan, P. A. van Aken and J. Maier, *Angew. Chem. Int. Ed.*, 2009, **48**, 6485.

33. B. Luo, B. Wang, M. Liang, J. Ning, X. Li and L. Zhi, *Adv. Mater.*, 2012, **24**, 1405.

34. K. T. Lee and J. Cho, *Nano Today*, 2011, **6**, 28.

35. C. Yuan, H. B. Wu, Y. Xie and X. W. Lou, *Angew. Chem. Int. Ed.*, 2014, **53**, 1488.

36. B. Wang, B. Luo, X. Li and L. Zhi, *Materials Today*, 2012, **15**, 544.

37. Y. Li, B. Tan and Y. Wu, *Nano Lett.*, 2008, **8**, 265.

38 L. Ji, Z. Tan, T. Kuykendall, E. J. An, Y. Fu, V. Battaglia and Yuegang Zhang, *Energy Environ. Sci.*, 2011, **4**, 3611.

# Chapter 2. Titanium oxide

## 2.1. Particle size control of $TiO_2$

### 2.1.1. Introduction

The insertion/extraction of Li ion into/from the $TiO_2$ can be expressed by the following reversible intercalation reactions:

$$TiO_2 + xLi^+ + xe^- \leftrightarrow Li_xTiO_2$$

$TiO_2$ with relatively high operation voltages are free from the formation of solid-electrolyte interface (SEI) layer which appears over most anode materials, such as graphite, Si, and Sn (below 0.5 V),[1,2] and makes batteries unstable and unsafe. The stability and long-lasting cycling property of $TiO_2$ result from the small volume changes (less than 4%) during the insertion/extraction of Li ion. Stability problems usually result from the substantial volume changes of active materials like Si, Sn, etc.[3,4] Thus, $TiO_2$ is increasingly gaining importance in the manufacturing of modern automobiles, such as hybrid or full electric vehicles (EVs), because of the advantages of $TiO_2$ over the conventional anode materials in stability and safety.[5-10]

When nanoparticles are utilized for LIB anode, the nanoparticle size is a very important factor in predicting the battery properties due to differences in surface area, contact conditions with the electrolyte, ion diffusion length, and so on. Although there

had been some reports on the effects of $TiO_2$ nanoparticles (TNPs) crystal size in LIB anode,[9] the polycrystalline particle size effect (not the crystal grain size but entire particle size composed of small crystal grains) had not yet been systemically studied. The effects of the crystal grain size upon Li ion insertion had been studied, and crystal grains as small as 7 nm were found to fully uptake the Li ion.[11] However, the $TiO_2$ crystal grains used in that study were commercial products obtained from different synthetic methods. Increasing Li ion capacity upon decrease of the crystal grain size from 30 nm to 6 nm was reported by another study, but the TNPs used were still from different commercial products.[12] The Kim group also researched the effects of crystal grain size of TNPs from the same synthetic procedure, using a different annealing temperature to control the crystal grain size.[13,14] However, annealing at different temperatures could not only vary the size of TNPs but could also change the crystal structure, which determines the electrochemical properties of particles, such as electric conductivity[15,16] and Li ion insertion mechanism.[10,17] However, researches on the size effect of TNPs were limited to the crystal grain size, and moreover, other factors like the crystalline structure and electric properties resulting from differences in the synthetic route were not controlled. Therefore, Li ion insertion of TNPs is still an important subject to be more methodically investigated under synthetically controlled conditions.

Herein, I investigated the electrochemical properties of the size-controlled anatase TNPs, with particle size of 60 nm, 120 nm, and 280 nm, respectively, assembled by

aggregation of crystallites about 12 nm, 12 nm, and 13 nm, respectively. Anatase TNPs of 60 nm size achieved Li ion capacity higher than the ideal capacity at 1 C and high rate performance without any additional processes or materials. We reported that the capacity activation is probably either due to the gradual penetration of electrolyte into the particles' interior and/or due to the lattice volume expansion of $TiO_2$. For the larger polycrystalline particle size, a longer contact period is required with the electrolyte into the particles' interior. Furthermore, the Li ion storage at high rate was more closely related to the surface area detected by Hg porosimetry analysis than to that detected by the more commonly used $N_2$ adsorption/desorption analysis, which provides an increased understanding of the actual contact area between solid active materials and liquid electrolyte especially at high current densities.

### 2.1.2. Experimental section

#### 2.1.2.1. Materials synthesis

For TNPs with 60 nm diameter, 0.5 mL of titanium butoxide was dissolved to 1:1 (v/v) mixture of anhydrous ethanol and acetonitrile (20 mL) in glove box. In round-bottom flask (RBF), 1:1 (v/v) mixture of ethanol and acetonitrile mixture (100 mL) with 1 mL of ammonia solution (29 % aqueous solution) was prepared. And then, prepared titanium butoxide solution was injected to RBF and the reaction was done under room temperature (RT). Synthesis of TNPs with 120 nm diameter was the same condition with 60 nm diameter synthesis except additional water was not used. In case of TNPs with 280 nm diameter, synthetic condition is as follows; 0.5 mL of titanium butoxide was dissolved to 1:1 (v/v) mixture of anhydrous ethanol and acetonitrile (20 mL) in glove box. In RBF, 1:1 (v/v) mixture of ethanol and acetonitrile mixture (100 mL) with 1 mL of ammonia solution (29 % aqueous solution) was prepared. And then, prepared titanium butoxide solution was injected to RBF and the reaction was done under RT. All TNPs - After 2 hours reaction, the whole milky solution of particles was purified and washed with ethanol using centrifugation/re-dispersion (17,000 rpm, 10 min, 3 times). The white product was well dried in RT for overnight, following annealed at 500 ℃ under air for 2 hours. Abbreviations will be used to indicate anatase TNPs: 60T for 60 nm TNPs, 120T for 120 nm TNPs, and 280T for 280 nm TNPs.

#### 2.1.2.2. Electrochemical measurement

Working electrodes were fabricated by mixing the size-controlled TNPs, Super P as a conductive agent, and PVDF as a binder in N-methyl-2-pyrrolidone (NMP) solvent at a weight ratio of 80:10:10. The mixed slurry was uniformly plastered on an aluminum foil current collector via doctor blade processing. The electrodes were dried under vacuum at 120 ℃ overnight and then pressed. A 2016 type coin cell consisted of a working electrode and lithium metal as a counter and reference electrode separated by a separator was assembled in a glove box under a dry argon atmosphere. The organic electrolyte used was 1.0 M $LiPF_6$ dissolved in a mixture of ethylene carbonate (EC) and diethyl carbonate (DEC) with a volume ratio of 1 : 1. Galvanostatic testing (WBCS3000 cycler, WonA tech, Korea) was carried out on the coin cell in the voltage range of 3.0 to 1.0 V (*vs.* $Li^+/Li$) at room temperature. The cyclic voltammetry (CV) was conducted at a scan rate of 0.1 mV/s. Scan rates for slow-scan cyclic voltammetry (SSCV) were varied from 0.1 to 1 mV/s to determine effective diffusion coefficient of $Li^+$.

#### 2.1.2.3. Characterization

The size and morphology of products were analyzed by field-emission scanning electron microscopy (FE-SEM, Hitachi S-4300, 4.2 kV) and transmission electron microscopy (TEM, Hitachi-7600, 100 kV). The crystallinity of the samples were evaluated by powder X-ray diffraction (XRD) analyses on Bruker New D8 Advance Diffractometer with Cu

Ka radiation (λ = 1.5418 Å). The scanning rate was 0.02 ° per second and range was from 10 to 70 °. The surface area and porosity of the products was measured using the nitrogen adsorption–desorption isotherm and BJH methods on a Micromeritics ASAP 2420. *In-situ* X-ray diffraction measurements were performed at the beam-line station 5A XRS-MS of the Pohang Accelerator Laboratory in Korea. A monochromatic X-ray beam with λ = 0.0765333 nm was transmitted through the thickness of a type 2032 coin cell. A hole was punched through each casing face, covered with a Kapton film to create an X-ray window for characterization.

### 2.1.3. Results and discussion

#### 2.1.3.1. Preparation of size-controlled $TiO_2$

Size control of TNPs from 60 nm to 300 nm was possible by varying the concentration of reactants (Fig. 2.1). Main factors changing the size of TNPs are concentration of water, ammonia solution and titanium source in each reaction conditions and they were investigated as follows. About 1:1 volume ratio of ethanol and acetonitrile seemed appropriate to prepare non-aggregated spherical TNPs with relatively narrow size distribution and the following synthesis of TNPs was proceeded using this condition.

Large-area HR-TEM images (Fig 2.2) show the almost remaining size about 60 nm, 120 nm and 280 nm, respectively and spherical shape of TNPs after calcination. More high-resolution images of only one-particle composed of small crystal grains also shown in Fig. 2.2.

Anatase phase of TNPs was confirmed by diffraction patterns from XRD. XRD patterns of three annealed TNPs also could be indexed to pure anatase phase (Fig. 2.3a). Moreover, from most intense (101) peak, crystal domain size of each anatase TNPs was calculated as 11.8 nm, 12.1 nm and 12.6 nm by scherrer equation, where the particle size from 60 nm, 120 nm and 280 nm, respectively.

The surface areas and pore distributions of the size-controlled anatase TNPs were investigated by using nitrogen adsorption/desorption isotherms as shown in Fig. 2.3b and summarized in Table 2.1. By using nitrogen-based BET first, the surface area of 60T was

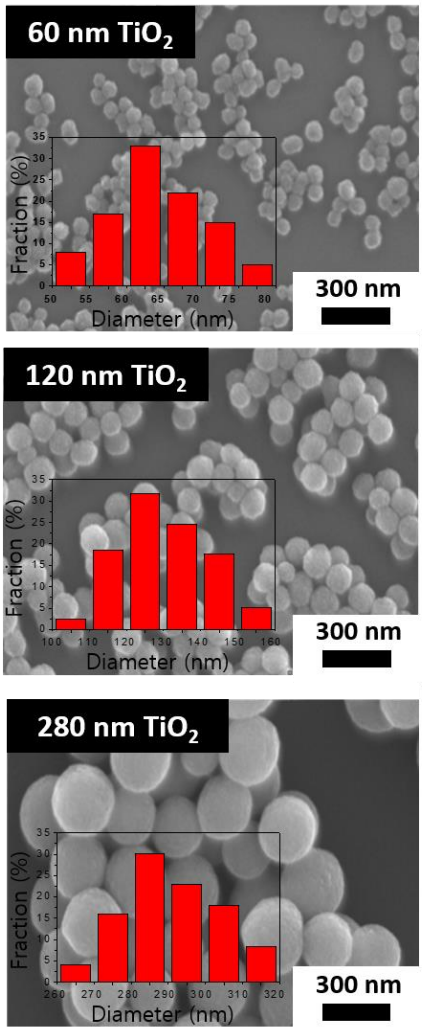


**Fig. 2.1** SEM images of size-controlled TNPs of the size range from about 60 nm to 300 nm.

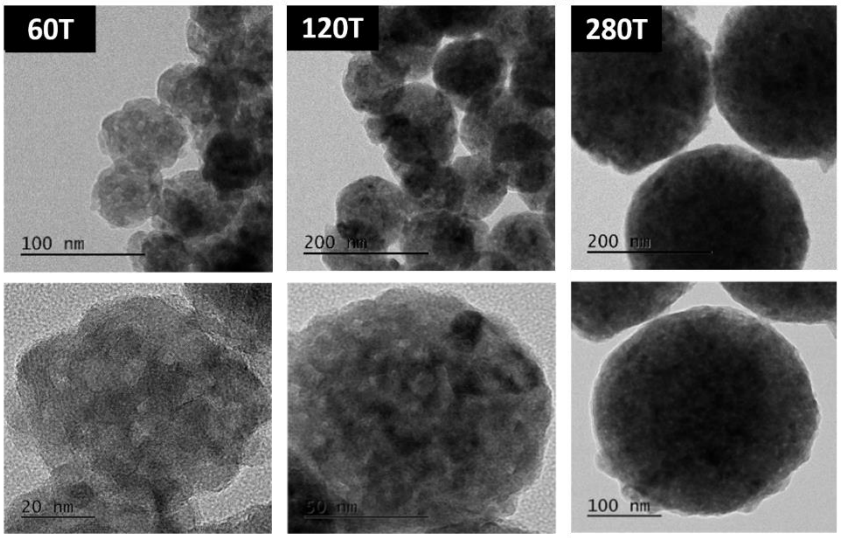


**Fig. 2.2** HR-TEM images of TNPs with the particle size of 60 nm, 120 nm, and 280 nm, respectively.

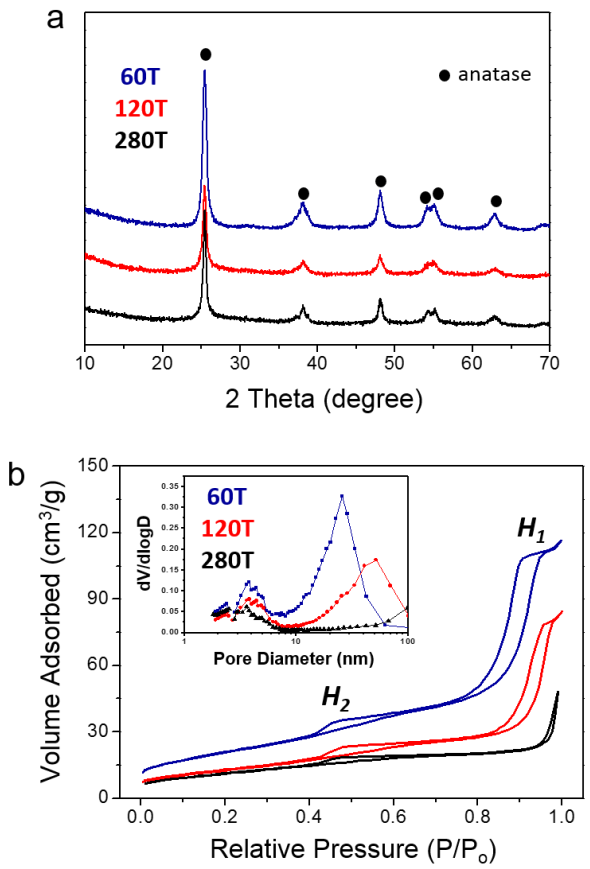


**Fig. 2.3** a) XRD patterns of TNPs and b) nitrogen adsorption/desorption isotherms of TNPs with the inset of BJH pore size distribution.

confirmed to be 73.1 $m^2/g$, which is higher than the 45.8 $m^2/g$ of 120T and the 40.9 $m^2/g$ of 280T. All TNPs showed type IV patterns in their isotherms, with distinct $H_1$ and $H_2$ hysteretic loops around 0.9 $P/P_0$ and 0.5 $P/P_0$, respectively[18] (Fig. 2.3b). The presence of $H_1$ loop characteristic is very interesting because it is expected to come from almost uniform TNPs spheres in a fairly regular array, and $H_2$ indicates the ink-bottle-type mesopores, which are typical of TNPs. This feature could be related to the pore size distribution resulting from the BJH method (the inset of Fig. 2.3b); all TNPs had pores as small as 4 nm and the smaller TNPs had more small-sized pores. The 60T and 120T had additional larger pores of 26 nm and 52 nm, respectively, which are believed to originate from the densely packed gaps between entire particles. Ideally, hexagonally close-packed identical 60 nm spheres have a cavity radius approximately 25 nm and 120 nm spheres have 50 nm,[19] which means that the size of inter-particle pores in this paper is very close to the calculated value. The 280T did not show any other large pores under 100 nm, but a pore larger than 100 nm (approximately 116 nm) is expected for the same reason as in the case of the other two TNPs. Because porous structures with bimodal pores are well known to have advantages in the adsorption of reactant molecules from fast diffusion,[20] 60T, which had the widest surface area and well developed bimodal pore, is expected to have good contact with LIB electrolyte.

Very similar measurements were also conducted by using mercury porosimetry. Although $N_2$-based detection of surface area and porosity is the generally used and

**Table 2.1** Structural properties of the size-controlled TNPs.

| TNPs | SSA (BET)[a] [$m^2/g$] | Small pore (BJH)[b] [nm] | Large pore (BJH) [nm] | SSA (Hg)[c] [$m^2/g$] | Small pore (Hg) [nm] | Large pore (Hg) [nm] | Interparticle pore[d] [nm] | Crystallite size (XRD)[e] [nm] | Particle size (TEM) [nm] |
|---|---|---|---|---|---|---|---|---|---|
| 60T | 73.1 | 4.3 | 25.7 | 32.4 | - | 13.6 | 24.8 | 11.8 | 60 |
| 120T | 45.8 | 4.3 | 51.6 | 17.4 | - | 21.2 | 49.7 | 12.1 | 120 |
| 280T | 40.9 | 4.3 | 100.6 | 6.3 | - | 40.4 | 115.9 | 12.6 | 280 |

[a]SSA = specific surface area; BET = Brunauer–Emmett–Teller,
[b]BJH = Barrett–Joyner–Halenda,
[c]SSA = specific surface area; Mercury Intrusion Porosimetry,
[d]determined by applying the Scherrer equation,
[e]calculated pore size from the hexagonal close packed sphere

accepted methodology, the material characteristics obtained from this method could not exactly explain the liquid-based contact between the solid anode and liquid electrolyte in LIBs. For example, gas can penetrate closed or small pores which a liquid electrolyte has difficulty entering. Even though the Hg-based method has disadvantages, such as less sensitivity on the nanometer scale due to the limited range of detection (from approximately 3-4 nm to 400-500 μm),[21,22] Hg liquid-based monitoring could still explain the contact between solid and liquid to support the $N_2$ gas-based method. Hg intrusion has been used to investigate the porous character of materials[22] and the changed porosity of Si anodes before and after lithiation,[23] but the Li ion capacity of materials could not be explained by this methodology. The surface areas of the TNPs were calculated with the Hg method to have lower numerical values than when $N_2$-based BET was used: 32.4 $m^2/g$ and 17.4 $m^2/g$ for 60T and 120T, respectively. Especially, notable is the very low surface area of 280T, 6.3 $m^2/g$, and the fact that these surface areas are lower than in $N_2$-based BET indicates that the Hg liquid could not intrude into small pores, such as micropores, small mesopores, and closed pores, and only gas could penetrate. Furthermore, the large pores from well-packed TNP aggregates were also found to be smaller than when the $N_2$-gased method was used-14 nm for 60T and 21 nm for 120T-demonstrating that intrusion of Hg liquid is more difficult than that of $N_2$ gas. The large pore of 280T was also detected to be 40 nm, which was not detected with $N_2$-based BJH. However, small pores of approximately 4 nm were not detected by $N_2$-based BJH, which

might result from the lower sensitivity on the several nanometer scale due to the limited detection range of the Hg porosimeter itself (could not detect under 3−4 nm) or the non-wetting character of Hg droplets.[21] The structural properties of commercially available $TiO_2$ nanoparticle powder were presented in Fig. 2.4.

#### 2.1.3.2. Electrochemical performance

The Li ion capacity of the size-controlled TNPs at a current density of 1 C (1 C = 168 mA/g) was evaluated as shown in Fig. 2.5a. The 60T demonstrates the best capacity and superior cycling stability with almost no fading up to 50 cycles. Moreover, the first discharge and charge capacities of 60T were 186 mAh/g and 179 mAh/g, which correspond to only 3.7% of the irreversible capacity loss (ICL). It is known that the ICL is possibly caused by side reactions, such as electrolyte decomposition, or by irreversible trapping of Li ions over the defects of anatase polymorph.[24] Without any additional materials enhancing conductivity or stability, the discharge capacity of 60T is comparable to recent researches which applied pure $TiO_2$ to anode material.[14,24,25] Fig. 2.5b shows the charge/discharge capacities of TNPs with the C-rate increasing from 0.5 C to 30 C. Clearly 60T indicates the best rate performance, not only with regard to capacity retention up to 80 cycles but also with regard to recovered capacity at 0.5 C after having increased to 30 C. The discharge capacity of 60T is 196 mAh/g and 193 mAh/g at the 10th and 80th cycles, which corresponds to almost 100% recovered capacity after the increase to 30 C.

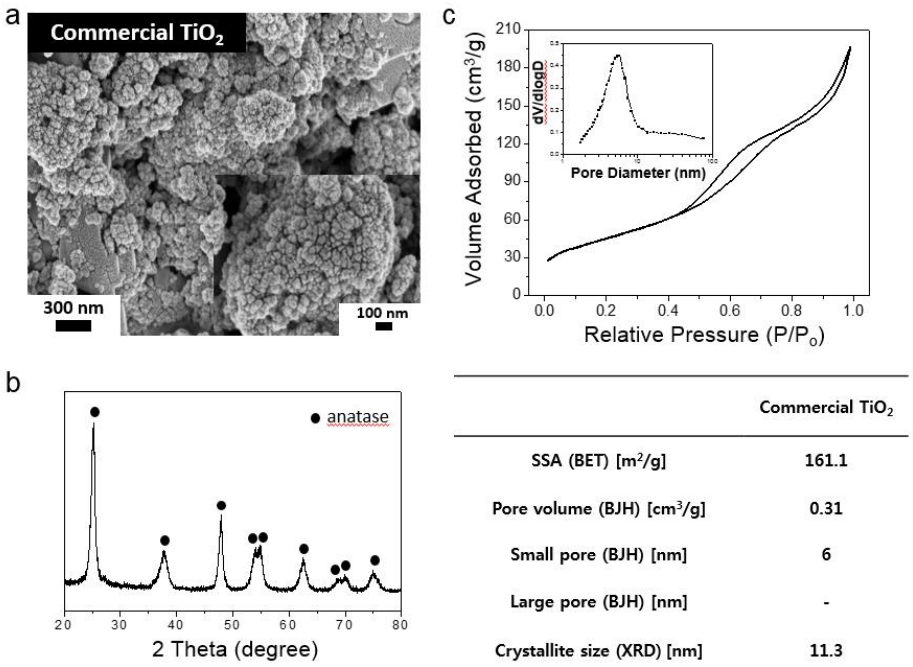


| | Commercial $TiO_2$ |
|---|---|
| SSA (BET) [$m^2/g$] | 161.1 |
| Pore volume (BJH) [$cm^3/g$] | 0.31 |
| Small pore (BJH) [nm] | 6 |
| Large pore (BJH) [nm] | - |
| Crystallite size (XRD) [nm] | 11.3 |

**Fig. 2.4** Structural properties of commercial $TiO_2$ nanopowder: a) SEM images, b) XRD patterns and c) nitrogen adsorption/desorption isotherms with the inset of BJH pore size distribution.

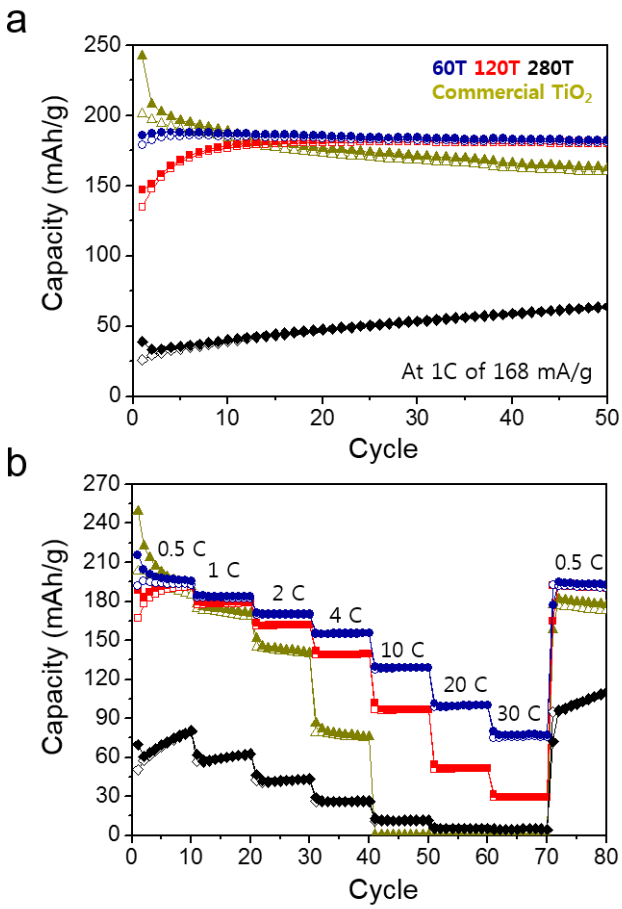


**Fig. 2.5** a) Cycle performance of the size-controlled TNPs and commercial $TiO_2$ at a current density of 168 mA/g at 1 C for 50 cycles and b) rate performance of the size-controlled TNPs and commercial $TiO_2$ at different current densities.

Furthermore, the discharge capacity of 60T at 10 C is 120 mAh/g, which is comparable to recent researches using defects or carbons,[26,27] or even better.[28,29] Compared with the size-controlled TNPs, unstable cycle retention was obtained in commercial $TiO_2$ electrode, showing a 20% capacity degradation. Also, the poor rate performance of commercial $TiO_2$ was presented in Fig. 2.5b.

It has been accepted that the insertion of Li ion into anatase $TiO_2$ is divided into three different regions:[30,31] solid-solution, intercalation, and surface adsorption (Region A, Region B, and Region C in Fig. 2.6, respectively). The first region of the discharge curve is characterized by a potential drop (> 1.78 V) which attributed to the formation of the conductive $Li_xTiO_2$ in the solid-solution domain. The second region exhibits a plateau at 1.78 V, which is well-known to be ascribed to two-phase electrochemical reactions. The third region (< 1.5 V) shows a sloped curve associated with further Li ion insertion into $Li_{0.5}TiO_2$ (i.e. interfacial storage process). A significant difference in the voltage profiles between 1st and 20th cycles is that the plateau potential gap between discharge and charge decreases considerably at the 20th cycle for all the TNPs. The degree of polarization of the electrode upon cycling decreases for all the TNPs, which indicates that Li ion insertion/extraction are easier upon cycling.[32] Furthermore, the discharge capacities of 120T and 280T are increased from 147 mAh/g and 39 mAh/g to 182 mAh/g and 54 mAh/g, respectively, at 30th cycle. Interestingly, the increase of capacity was observed for all the TNPs in Fig. 2.5. This increasing capacity character of TNPs was further

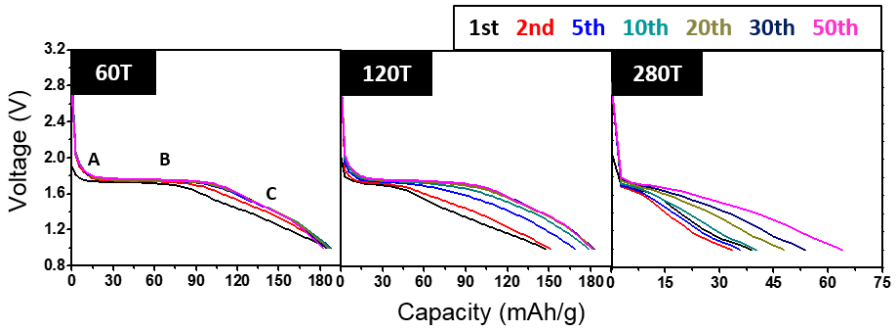


**Fig. 2.6** Insertion curves of TNPs at the selected cycles.

evaluated because it was rarely reported and not well understood yet. There are several proposed explanations of the increased capacity upon cycling. The first is reversible growth of a polymer or gel-like thin film layer resulting from the decomposition of electrolyte on the surface of anode materials. However, this layer is usually formed at low voltage, around 0.8 V, and $TiO_2$ is well known to hardly form at decomposed thin layer at relatively high operating voltages of 1.5−1.8 V.[5,33-35] The second proposal is the recovered capacity from the irreversibly reacted and unused portions of anodes during the initial cycles. Yu *et al.*[36] and Lian *et al.*[37] insisted that the initial irreversible capacity via the conversion reaction was becoming partially reversible with repeated cycling. This proposal could describe the behavior of active materials that react with Li ion through conversion reactions, such as $SnO_2$ and other metal oxide systems.[36,37] However, this proposal also could not explain the answer of increasing capacity of $TiO_2$, which takes Li ion by an intercalation mechanism. $TiO_2$ is well known as a very stable material for LIB anodes, mainly due to its low volume change during charging/discharging processes. The lattice volume of $TiO_2$ would expand only approximately 3−4% upon repeated intercalation reactions.[30,31,38] Moreover, from the 1% lattice expansion of $Li_4Ti_5O_{12}$, Li ion diffusivity could increase by one order of magnitude.[39] Fig. 2.7−9 of *in-situ* synchrotron XRD patterns show the slight lattice expansion on intercalation. Fig. 2.7 and 2.8 indicate the two-phase reaction in 60T with the Li-poor anatase $TiO_2$ phase ($\alpha \sim 0.026$) and the Li-rich Li titanate phase ($\beta \sim 0.55$),[40] and the formation of conductive

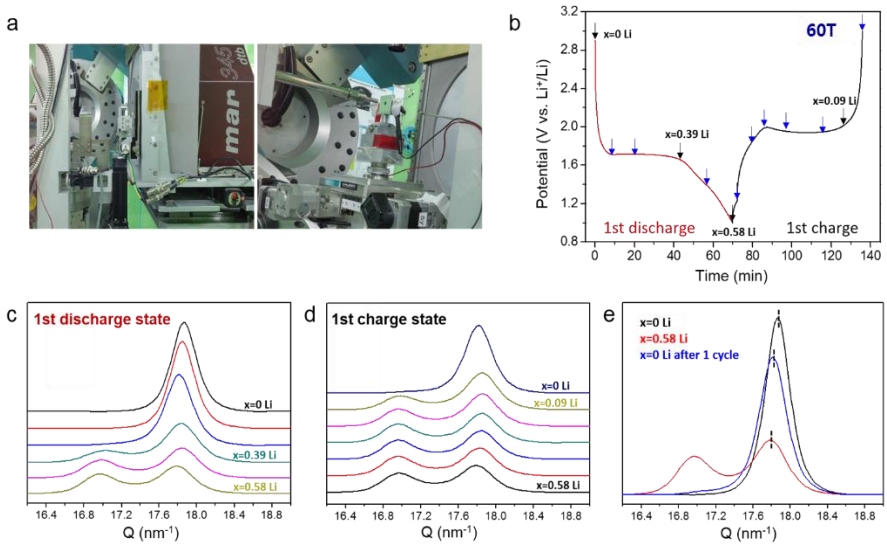


**Fig. 2.7** a) Photograph of *in-situ* XRD equipment, b) discharge and charge curves of 60T at the first cycle, and c)-e) *in-situ* synchrotron XRD patterns.

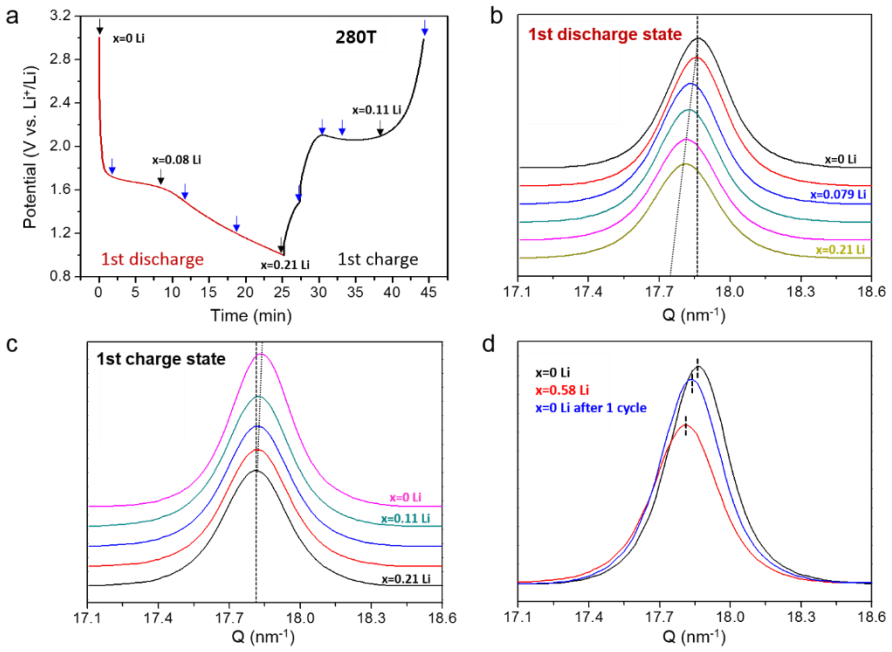


**Fig. 2.8** a) Discharge and charge curves of 280T at the first cycle and b)-d) *in-situ* synchrotron XRD patterns.

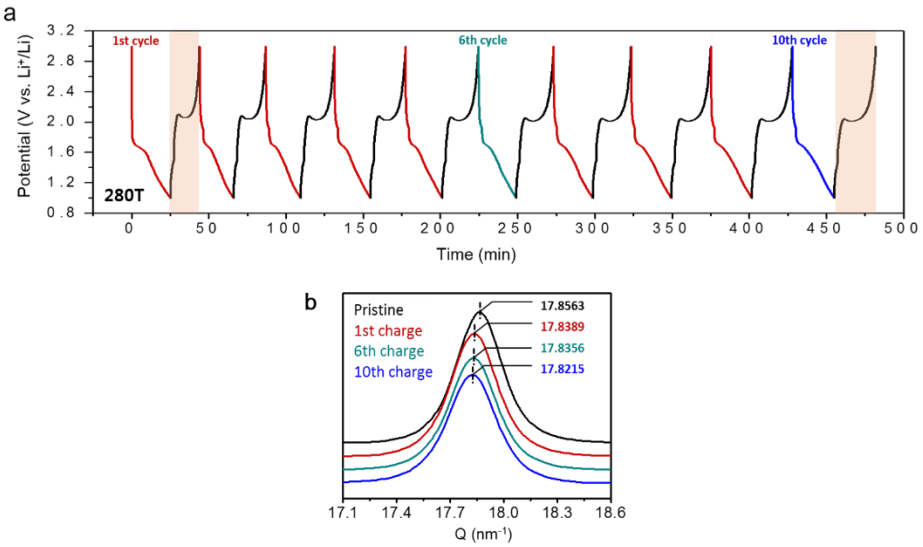


**Fig. 2.9** a) Voltage profiles of 280T during 10 cycles and b) *in-situ* synchrotron XRD patterns at selected charge state.

$Li_xTiO_2$ in 120T, respectively. In particular, a slight shift of the peaks to lower scattering vectors, corresponding to the slight lattice expansion even after the charging process, is observed in both Fig. 2.7e and 2.8d. Moreover, the peak shifts to lower scattering vectors upon cycling, as shown in Fig. 2.9. Therefore, the improved capacity is probably either due to gradual penetration of electrolyte into the particles' interior[41] and/or due to lattice volume expansion of $TiO_2$, which enables further electrolyte penetration. In addition, the faster increasing capacity of 120T than 280T might come from both higher surface area and more porous structure providing sufficient electrode/electrolyte contact and facile Li ion transport. Moreover, the utilization of Region B increases upon cycling in both 60T and 120T and saturates at the 10th and 20th cycle as shown in Fig. 2.10, implying the intercalation reaction is depend on particle size at initial stage of the whole cycles. It is well known that crystal grain size strikingly impacts on the Li ion insertion behavior and storage capability.[11,13,14,30] From the particle size-dependent electrochemical behavior, polycrystalline particle size as well as crystal grain size affects the Li ion storage capability; the larger entire particle size of 120T could not showed its highest capacity until 20th cycle, suggesting that the longer period to contact with electrolyte into the particles' interior is required for the larger polycrystalline particle size.

To investigate Li ion diffusion both in active materials and in the electrolyte near the interface between the electrolyte and electrode, CV measurements with varying scanning rates of 0.1, 0.2, 0.3, 0.4, 0.5, and 1 mV/s were conducted, as shown in Fig. 2.11. By using

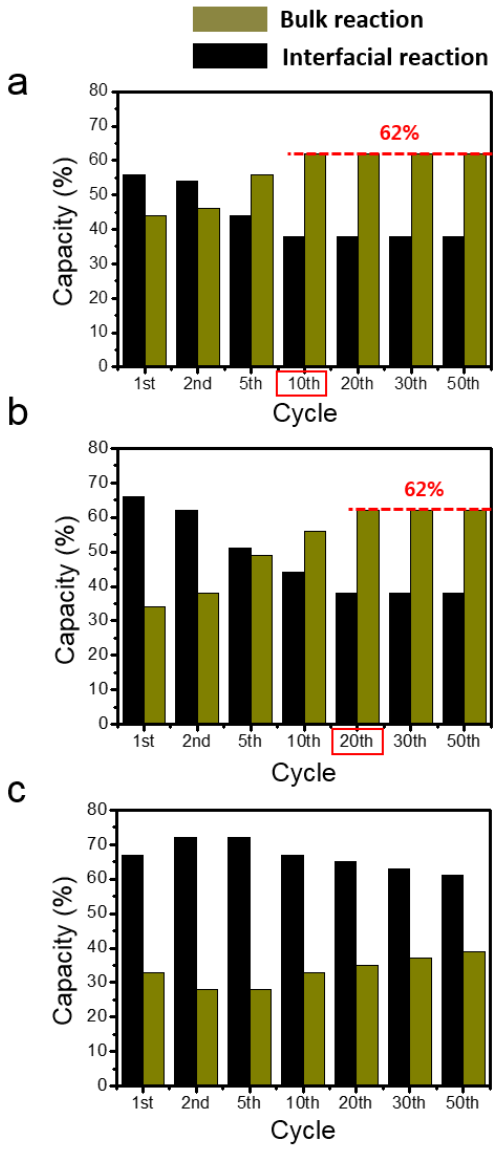


**Fig. 2.10** Bar graphs of insertion capacities of a) 60T, b) 120T, and c) 280T at selected cycles.

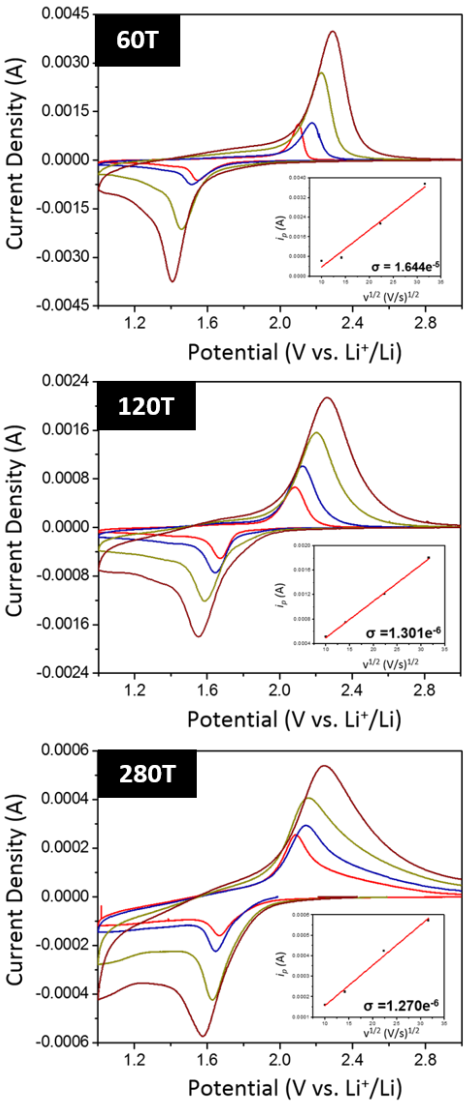


**Fig. 2.11** SSCVs of a) 60T, b) 120T, and c) 280T. The correlation line of $i_p$ *vs.* $v^{1/2}$ is displayed in the inset.

the Randles–Sevcik equation for the reversible diffusion-controlled system at room temperature, the diffusion coefficient (*D*) could be obtained via the slope from the voltammetric current densities *vs*. the square root of the scan rate.[42] The equation is

$$i_p = (2.69 \times 10^5) n^{3/2} A D^{1/2} C v^{1/2}$$

,where $i_p$ is the peak current, $n$ is the number of electrons transferred in the electrode reaction, $A$ is the surface area of the electrode ($cm^2$), $D$ is diffusion coefficient of Li ion ($cm^2/s$), $C$ is the concentration of Li ion ($mol/cm^3$), and $v$ is the CV scan rate (V/s). As discussed above, because the detected surface area of the TNPs has different values depending upon the physical phase of the medium (e.g. gas or liquid) used for analysis, plausible surface areas of the TNPs are necessary to obtain the effective $D_{Li+}$. The determined $D_{Li+}$ of 60T is $8.12 \times 10^{-20}$ $cm^2/s$ in accordance with the recently reported value estimated by the SSCV method,[43] and the $D_{Li+}$ increased with decreasing TNP size. Generally, the mobility of electrons is faster than that of Li ion, hence Li ion diffusion has practical importance for achieving high LIB performance. Therefore, the results attribute the best electrochemical performance of 60T among the TNPs to fast Li ion diffusion kinetics.

Fig. 2.12a presents the last discharge curves of each cycle set in Fig. 2.5b of 60T at various rates. It is well known that the extent of both Region A and C depends on the

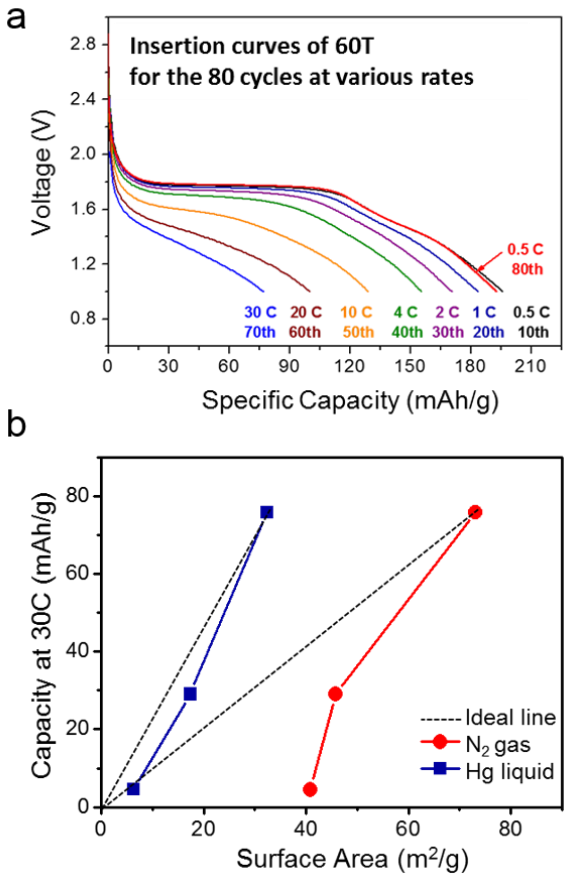


**Fig. 2.12** a) The 1st insertion curves of 60T at rates from 0.5 C to 30 C and b) relation between discharge capacity at 30 C and surface area from $N_2$ method (red solid) and Hg method (blue solid) compared to the ideal line (black dotted).

surface area of the material[5,14,25,44] and the proportion of Region C in the overall discharge capacity significantly increased as the C-rate increased. This result implied that the reaction kinetics of surface adsorption is much faster than those of intercalation reactions, and thus, high rates might provide more emphasis on the surface area dependent storage mechanisms.[32,44] Based on discussions and references above, the capacity at high rate is related with the surface area of TNPs. From $N_2$ adsorption/desorption analysis, the highest surface area was obtained in 60T and comparatively similar surface area was developed in 120T and 280T. But the capacity gap between each TNP is similar showing stair-like differences and it is more related with the surface area characterized via Hg intrusion porosimetry. The relation between the discharge capacity at 30 C and the surface areas characterized both the $N_2$ adsorption/desorption analysis and Hg intrusion porosimetry analysis depicted in Fig. 2.12b. If TNPs with very small surface area could be assumed to have no Li ion storage at high current density of 30 C, the black dotted line might indicate the ideal linear-relation between Li ion capacity with surface area of TNPs for each analysis. The plot from Hg liquid analysis shows more similar relation with ideal line than from $N_2$ gas analysis, proposing that it is another helpful tool understanding the contact area between solid active materials and liquid electrolytes especially at high current density.

### 2.1.4. Conclusions

A simple sol-gel method using a solvent mixture of ethanol and acetonitrile had been introduced to prepare size-controlled TNPs even with sizes under 100 nm, which had not been reported in studies using similar methods. Three anatase TNPs were synthesized, which had diameters of 60 nm, 120 nm, and 280 nm (notated as 60T, 120T, and 280T, respectively), and were assembled by aggregation of crystallites of approximately 12 nm, 12 nm, and 13 nm, respectively. The 60T electrode exhibited good Li ion storage performance, showing a large reversible capacity of 182 mAh/g during 50 cycles at 1 C and a remarkable rate performance of 120 mAh/g at 10 C. All the TNPs presented capacity activation, and we propose that this phenomenon is either due to the gradual penetration of electrolyte into the particles' interior and/or due to the lattice expansion upon cycling. We demonstrated that Hg porosimetry analysis could more accurately describe the actual contact area between solid active materials and liquid electrolyte than the areas from $N_2$ adsorption/desorption analysis, especially at high rate.

*** Contributions**

The synthesis of size-controlled $TiO_2$ nanoparticles was designed with JooHyun Lim and Prof. Jin-Kyu Lee in Department of Chemistry, Seoul National University.

## 2.2. References


1. X. Chen, S. S. Mao, *Chem. Rev.* **2007**, *107*, 2891.

2. D. Chen, R. A. Caruso, *Adv. Funct. Mater.* **2013**, *23*, 1356.

3. Q. Zhang, E. Uchaker, S. L. Candelaria, G. Cao, *Chem. Soc. Rev.* **2013**, *42*, 3127.

4. W. Li, Z. Wu, J. Wang, A. A. Elzatahry, D. Zhao, *Chem. Mater.* **2014**, *26*, 287.

5. Z. Chen, I. Belharouak, Y. K. Sun, K. Amine, *Adv. Funct. Mater.* **2013**, *23*, 959.

6. M. V. Reddy, G. V. Subba Rao, B. V. Chowdari, *Chem. Rev.* **2013**, *113*, 5364.

7. T. Froschl, U. Hormann, P. Kubiak, G. Kucerova, M. Pfanzelt, C. K. Weiss, R. J. Behm, N. Husing, U. Kaiser, K. Landfester, M. Wohlfahrt-Mehrens, *Chem. Soc. Rev.* **2012**, *41*, 5313.

8. X. Su, Q. Wu, X. Zhan, J. Wu, S. Wei, Z. Guo, *J. Mater. Sci.* **2012**, *47*, 2519.

9. C. H. Jiang, J. S. Zhang, *J. Mater. Sci. Technol.* **2013**, *29*, 97.

10. Z. Yang, D. Choi, S. Kerisit, K. M. Rosso, D. Wang, J. Zhang, G. Graff, J. Liu, *J. Power Sources* **2009**, *192*, 588.

11. M. Wagemaker, W. J. H. Borghols, F. M. Mulder, *J. Am. Chem. Soc.* **2007**, *129*, 4323.

12. C. Jiang, M. Wei, Z. Qi, T. Kudo, I. Honma, H. Zhou, *J. Power Sources* **2007**, *166*, 239.

13. J. W. Kang, D. H. Kim, V. Mathew, J. S. Lim, J. H. Gim, J. Kim, *J. Electrochem. Soc.* **2011**, *158*, A59.

14. A. K. Rai, L. T. Anh, J. Gim, V. Mathew, J. Kang, B. J. Paul, J. Song, J. Kim, *Electrochim. Acta* **2013**, *90*, 112.

15. A. Tighineanu, T. Ruff, S. Albu, R. Hahn, P. Schmuki, *Chem. Phys. Lett.* **2010**, *494*, 260.

16. H.-T. Fang, M. Liu, D.-W. Wang, T. Sun, D.-S. Guan, F. Li, J. Zhou, T.-K. Sham, H.-M. Cheng, *Nanotechnology* **2009**, *20*, 225701.

17. D. Deng, M. G. Kim, J. Y. Lee, J. Cho, *Energy Environ. Sci.* **2009**, *2*, 818.

18. K. S. W. Sing, *Pure Appl. Chem.* **1985**, *57*, 603.

19. R. G. Avery, J. D. F. Ramsay, *J. Colloid Interface Sci.* **1973**, *42*, 597.

20. Y. Chen, D. D. Dionysiou, *Appl. Catal., B* **2008**, *80*, 147.

21. H. Giesche, *Part. Part. Syst. Charact.* **2006**, *23*, 9.

22. G. Tzschichholz, G. Steinborn, M. P. Hentschel, A. Lange, P. Klobes, *J. Porous Mater.* **2011**, *18*, 83.

23. M. R. Jo, Y.-U. Heo, Y. C. Lee, Y.-M. Kang, *Nanoscale* **2014**, *6*, 1005.

24. Y. Ma, G. Ji, B. Ding, J. Y. Lee, *J. Mater. Chem.* **2012**, *22*, 24380.

25. P. Kubiak, T. Fröschl, N. Hüsing, U. Hörmann, U. Kaiser, R. Schiller, C. K. Weiss, K. Landfester, M. Wohlfahrt-Mehrens, *Small* **2011**, *7*, 1690.

26. Z. H. Bi, M. P. Paranthaman, B. K. Guo, R. R. Unocic, H. M. Meyer, C. A. Bridges, X. G. Sun, S. Dai, *J. Mater. Chem. A* **2014**, *2*, 1818.

27. M. M. Zhen, L. W. Su, Z. H. Yuan, L. Liu, Z. Zhou, *RSC Adv.* **2013**, *3*, 13696.

28. W. Jiao, N. Li, L. Wang, L. Wen, F. Li, G. Liu, H.-M. Cheng, *Chem. Commun.* **2013**, *49*, 3461.

29. C. L. Zhang, Q. Y. Zhang, S. F. Kang, X. Li, *J. Mater. Chem. A* **2014**, *2*, 2801.

30. M. Wagemaker, G. J. Kearley, A. A. van Well, H. Mutka, F. M. Mulder, *J. Am. Chem. Soc.* **2002**, *125*, 840.

31. J. Wang, Y. Zhou, Y. Hu, R. O'Hayre, Z. Shao, *J. Phys. Chem. C* **2011**, *115*, 2529.

32. J. F. Lei, K. Du, R. H. Wei, J. Ni, L. B. Li, W. S. Li, *RSC Adv.* **2013**, *3*, 13843.

33. C. Ban, Z. Wu, D. T. Gillaspie, L. Chen, Y. Yan, J. L. Blackburn, A. C. Dillon, *Adv. Mater.* **2010**, *22*, E145.

34. J. E. Lee, S.-H. Yu, D. J. Lee, D.-C. Lee, S. I. Han, Y.-E. Sung, T. Hyeon, *Energy*

*Environ. Sci.* **2012**, *5*, 9528.

35. P. L. Taberna, S. Mitra, P. Poizot, P. Simon, J. M. Tarascon, *Nat. Mater.* **2006**, *5*, 567.

36. Y. Yu, C. H. Chen, Y. Shi, *Adv. Mater.* **2007**, *19*, 993.

37. P. Lian, X. Zhu, S. Liang, Z. Li, W. Yang, H. Wang, *Electrochim. Acta* **2011**, *56*, 4532.

38. M. Zukalová, M. Kalbáč, L. Kavan, I. Exnar, M. Graetzel, *Chem. Mater.* **2005**, *17*, 1248.

39. K. Song, D.-H. Seo, M. R. Jo, Y.-I. Kim, K. Kang, Y.-M. Kang, *J. Phys. Chem. Lett.* **2014**, *5*, 1368.

40. K. Shen, H. Chen, F. Klaver, F. M. Mulder, M. Wagemaker, *Chem. Mater.* **2014**, *26*, 1608.

41. X.-L. Wu, L.-Y. Jiang, F.-F. Cao, Y.-G. Guo, L.-J. Wan, *Adv. Mater.* **2009**, *21*, 2710.

42. M. Bousa, B. Laskova, M. Zukalova, J. Prochazka, A. Chou, L. Kavan, *J. Electrochem. Soc.* **2010**, *157*, A1108.

43. J.-Y. Shin, J. H. Joo, D. Samuelis, J. Maier, *Chem. Mater.* **2011**, *24*, 543.

44. J.-Y. Shin, D. Samuelis, J. Maier, *Adv. Funct. Mater.* **2011**, *21*, 3464.

# Chapter 3. Tin oxide

## 3.1. Tin oxide coated three-dimensional copper foam

### 3.1.1. Introduction

Tin dioxide ($SnO_2$) has been regarded as a promising alternative to the currently used graphite anode for next generation lithium-ion batteries (LIBs) because of its relatively low cost, low toxicity, high natural abundance, and, most importantly, low discharge potential and high theoretical capacity of 781 mAh $g^{-1}$ from the maximum reaction to form $Li_{4.4}Sn$ alloy.[1-3] However, the large amounts of Li ions inserted/extracted into/from Sn induce severe volume changes (up to approximately 300%), which causes a pulverization of Sn particles and a loss of electrical contact with current collector, eventually resulting in poor electrochemical performance.[2-4]

Substantial efforts have been devoted to addressing this issue, and two approaches have been extensively investigated: a unique nanostructuring of $SnO_2$ for short Li ion diffusion paths and void spaces to accommodate the severe volume changes[4,5] and a nanocompositing with carbonaceous materials for enhanced electrical conductivity and structural stability resulted from the coating layer or matrix.[4,6] However, the introduction of carbonaceous materials into $SnO_2$ has an inherent weakness with respect to gravimetric specific capacity calculated from the combination of $SnO_2$ and carbon. Since the theoretical capacity of graphite, based on a reversible intercalation reaction, is 372 mAh

$g^{-1}$ (corresponding to $LiC_6$) which is considerably lower than that of $SnO_2$. Although in case of graphene the theoretical capacity is 740 mAh $g^{-1}$ (corresponding to $Li_2C_6$) which is limited to the carbon composed predominantly of single layers.[7,8] Therefore, the unique morphology controls of $SnO_2$ using several synthetic methods have been proposed to achieve prolonged cycle stability without a decrease in the gravimetric specific capacity. Many researches for the morphology controls of $SnO_2$ have been accomplished, including one-dimensional (1D) nanorods,[9] nanotubes,[10] or nanowires,;[11,12] two-dimensional (2D) nanosheets,;[13,14] and three-dimensional (3D) nanoarchitectures.[15] Recently, the 3D scaffold architecture has attracted attention as a smart electrode prototype,[16,17] and various architectures from simple periodic arrays of cylindrical nanopillars[18] to complex arrangements such as inverse opal scaffold,[19] foams,[20,21] and long chains of particles[22] have been conducted.

Herein, I report a facile synthesis of $SnO_2$-coated Cu foam ($SnO_2$/Cu foam) as a self-supporting anode for LIBs. Through the use of a simple sol-gel method, a $SnO_2$/Cu foam integrated with current collector, and free of binder and conducting agent was obtained. The $SnO_2$/Cu foam exhibited a high reversible capacity of 621 mAh $g^{-1}$ at a rate of 1 C after 50 cycles, an excellent rate capability of 368 mAh $g^{-1}$ at 2 C, and a stable cycle performance, and its structural integrity was preserved after cycling.

### 3.1.2. Experimental section

#### 3.1.2.1. Materials synthesis

A tin oxide-based sol was prepared by dissolving 0.338 g of $SnCl_2 \cdot 2H_2O$ in a solvent mixture consisting of 0.03 mL 37% hydrochloric acid and 0.47 mL ethanol to obtain a 3 M Sn(II) solution,[23] which was subsequently aged at room temperature for 24 h. Triple deionized water (DI-$H_2O$) was then added to the solution, which was aged for another 24 h. Commercially available Cu foam (purchased from Korea Metalfoam company) was punched 11 mm in diameter to fit electrode size and immersed in the prepared gel for 24 h. Solvent evaporation was then conducted at 80 °C in vacuum. A heat treatment was carried out at 500 °C under Ar atmosphere for 2 h to convert the tin oxide precursor gel into crystalline $SnO_2$ and to obtain final product as an electrode. For the comparison of sol-gel concentration effect on electrochemical performance, the $SnO_2$-coated Cu foam ($SnO_2$/Cu foam) from a 10 M Sn(II) solution was prepared by the same experimental procedure (1.128 g of $SnCl_2 \cdot 2H_2O$ in a solvent mixture consisting of 0.03 mL 37% hydrochloric acid and 0.47 mL ethanol as a 10 M Sn(II) solution). $SnO_2$/Cu foams from 3 M and 10 M were referred to as $SnO_2$/Cu foam@3M and $SnO_2$/Cu foam@10M, respectively, and electrochemically tested.

#### 3.1.2.2. Electrochemical measurements

The $SnO_2$/Cu foam was directly used as a working electrode and assembled into a coin cell without the addition of any binding or conductive materials, and was compared with a $SnO_2$ powder electrode ($SnO_2$ NPs) as control. Commercial $SnO_2$ powder (<100 nm, purchased from Aldrich) was mixed with Ketchen Black as a conductive agent and PVDF in N-methyl-2-pyrrolidone solvent as a binder. The $SnO_2$ powder : Ketchen Black : PVDF weight ratio was 80:10:10. The mixed slurry was uniformly plated onto Cu foil as a current collector by using a doctor blade method. The electrode was dried under vacuum at 120 °C for 8 h and was then pressed at room temperature. A 2032-type coin cell, consisting of the $SnO_2$/Cu foam as the working electrode, lithium metal as both the counter and reference electrodes, and a polypropylene separator, was assembled in a glove box under Ar. The electrolyte used in this study was 1.0 M $LiPF_6$ dissolved in a mixture of ethylene carbonate (EC) and diethyl carbonate (DEC) in a volume ratio of 1 : 1. A galvanostatic test (WBCS3000 cycler, WonA Tech, Korea) was carried out.

**3.1.2.3. Characterization**

XRD patterns were obtained on a Bruker D-5005 with Cu Kα radiation (λ = 1.5406 Å) operating at 40 kV and 40 mA with a scan range of 20–80°. The morphologies of specimens were characterized by carrying out field emission scanning electron microscopy (FE-SEM, Hitachi S-4800). FE-SEM images using focused ion beam (FIB) milling were taken with Carl Zeiss SUPRA 55VP and Carl Zeiss AURIGA.

### 3.1.3. Results and discussion

#### 3.1.3.1. Preparation of $SnO_2$-coated Cu foam

The surface morphologies of commercially available Cu foam in the pristine state (Fig. 3.1a-c) and after $SnO_2$ sol-gel coating (Fig. 3.1d-f) were shown in Fig. 3.1. In Fig. 3.1a, prior to coating with $SnO_2$, the Cu foam was a 3D interconnected scaffold composed of continuous struts with a width of less than approximately 100 μm and of interconnected pores with a diameter of 100−500 μm. This morphology character is also confirmed at lower magnification in the inset of Fig. 3.1a. The surface of the struts was further examined using higher magnification FE-SEM images (Fig. 3.1b and c), and the development of small pores and grains on the surface was observed. After $SnO_2$ coating, the 3D interconnected scaffold of the Cu foam was maintained as shown in Fig. 3.1d, and the surface morphology of the Cu foam was relatively smooth with covering the small pores and the grains (Fig. 3.1e and f).

Fig. 3.2a-d present FE-SEM and EDX mapping images of the Cu foam after $SnO_2$ coating. The presence of Cu, Sn, and O was confirmed, and the distributions of Sn and O corresponded with that of Cu, which implies that the Cu foam served as a template for the deposition of $SnO_2$. To confirm the thickness of the $SnO_2$ deposited as a coating layer, the cross-sectional image of Fig. 3.2a obtained using FIB milling is presented in Fig. 3.2e. The inset shows a whole cross-sectional image of the $SnO_2$/Cu foam, and the magnified image indicates that the Cu foam was covered with a thin (approximately 200 nm) and

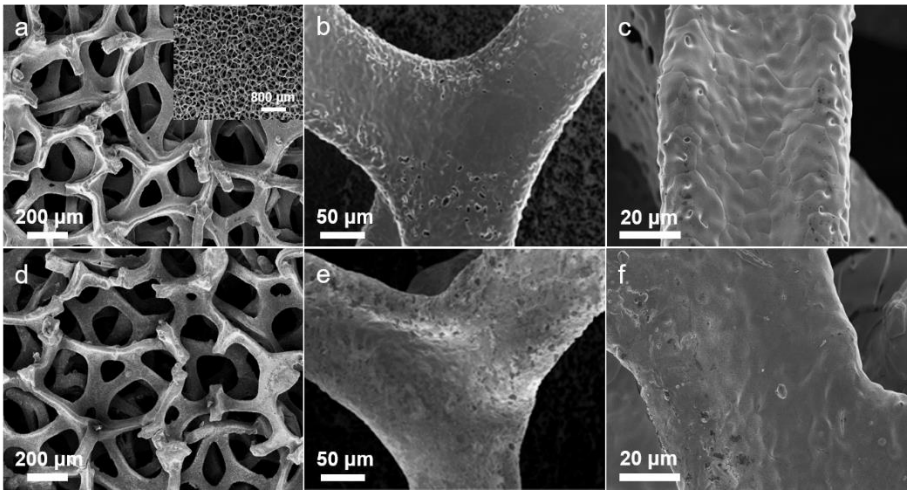


**Fig. 3.1** FE-SEM images of Cu foam at pristine state (a)-(c) and after $SnO_2$ sol-gel coating (d)-(f). The inset shows the pristine Cu foam at low magnification.

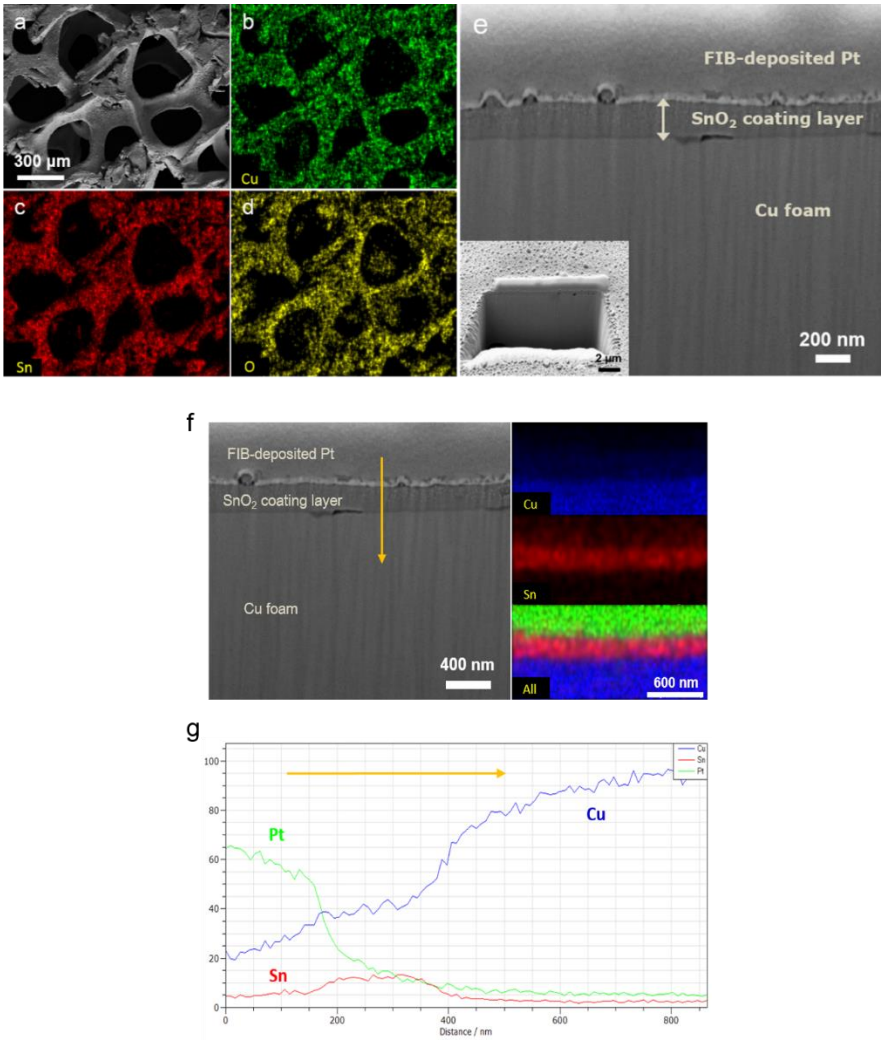


**Fig. 3.2** FE-SEM images of $SnO_2$-coated Cu foam using EDX mapping (a)-(d) and using FIB milling (e), (f) SEM and EDX mapping images of $SnO_2$/Cu foam after FIB milling, and (g) EDX line scan result across the $SnO_2$ coating layer as indicated by the arrow direction.

uniform layer. This coating layer is presumed to be a $SnO_2$ based on the EDX mapping (Fig. 3.2f), and its thickness of approximately 200 nm was confirmed from the EDX line scan (Fig. 3.2g). The XRD pattern in Fig. 3.3 confirms the presence of the $SnO_2$ because only peaks for tetragonal rutile $SnO_2$ (JCPDS 41-1445) and metallic Cu (JCPDS 04-0836) are observed with no additional peaks such as SnO and $Cu_2O$.[24-26]

### 3.1.3.2. Electrochemical performance

The $SnO_2$ sol-gel concentration was initially investigated under the assumption that the Sn(II) molar concentration may or may not have an impact on the electrochemical performance. $SnO_2$/Cu foams were prepared from different Sn(II) molar concentrations of 3 M and 10 M, and these foams were referred to as $SnO_2$/Cu foam@3M and $SnO_2$/Cu foam@10M, respectively. To understand the reactive processes of the $SnO_2$/Cu foam@3M and $SnO_2$/Cu foam@10M, cyclic voltammetry (CV) measurement was conducted in the voltage range of 0.01–2 V at a scan rate of 0.1 mV $s^{-1}$ (Fig. 3.4a and b). The first five CV curves of $SnO_2$/Cu foam@3M and $SnO_2$/Cu foam@10 M were in accord with the electrochemical behaviour of $SnO_2$-based materials.[27-29] The first cathodic peak at 0.64 V of the $SnO_2$/Cu foam@3M is ascribed to the irreversible formation of a solid electrolyte interface (SEI) layer due to electrolyte decomposition and the reduction of $SnO_2$ to Sn as followed by eqn (1) and (2), respectively.

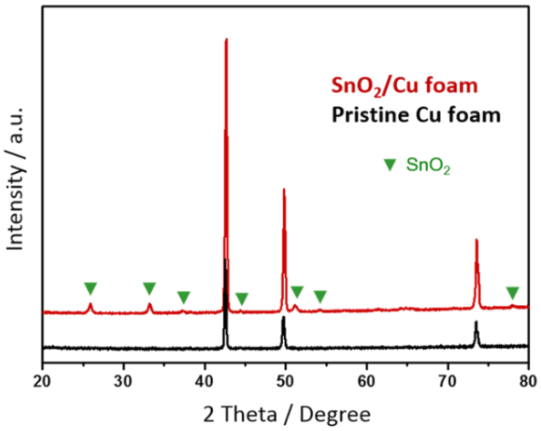


**Fig. 3.3** XRD patterns of pristine Cu foam and $SnO_2$/Cu foam after heat treatm ent at 500 under Ar atmosphere.

$$Li^+ + e^- + \text{electrolyte} \rightarrow \text{SEI (Li)} \quad (1)$$

$$SnO_2 + 4Li^+ + 4e^- \rightarrow Sn + 2Li_2O \quad (2)$$

$$Sn + xLi^+ + xe^- \rightarrow Li_xSn \quad (0 \leq x \leq 4.4) \quad (3)$$

In addition, the cathodic peaks at 0.0–0.5 V indicate the formation of $Li_xSn$ alloys as described by eqn (3), and the corresponding anodic peaks appeared at 0.2–1.0 V because of the extraction of Li ions from the LixSn alloys.[30] The anodic peak appeared at 1.42 V, which is attributed to the oxidation of Sn to $SnO_2$, and the first cathodic peak shifted to higher voltages by around 0.94 V during subsequent cycles, which implies partial reversibility of the electrochemical reaction described by eqn (2).[29,31] A battery performance test was carried out to examine the potential of $SnO_2$/Cu foam@3M and $SnO_2$/Cu foam@10M as anode for LIBs. Fig. 3.4c presents the first two voltage profiles of $SnO_2$/Cu foam@3M and $SnO_2$/Cu foam@10M in the voltage range of 0.01–2 V at a current density of 1 C (1 C = 781 mA $g^{-1}$), and these voltage profiles are consistent with the corresponding CV curves (Fig. 3.4 a and b) and with the lithiation/delithiation process described in previous reports.[22,31] The cycling performances of $SnO_2$/Cu foam@3M and $SnO_2$/Cu foam@10M at 1 C are shown in Fig. 3.4d. Both electrodes exhibited stable capacity retention, and the capacity of $SnO_2$/Cu foam@10M was approximately 200 mAh $g^{-1}$ higher than that of $SnO_2$/Cu foam@3M throughout all of the cycles. Although the reason for the increase in capacity with increasing Sn(II) molar concentration is not

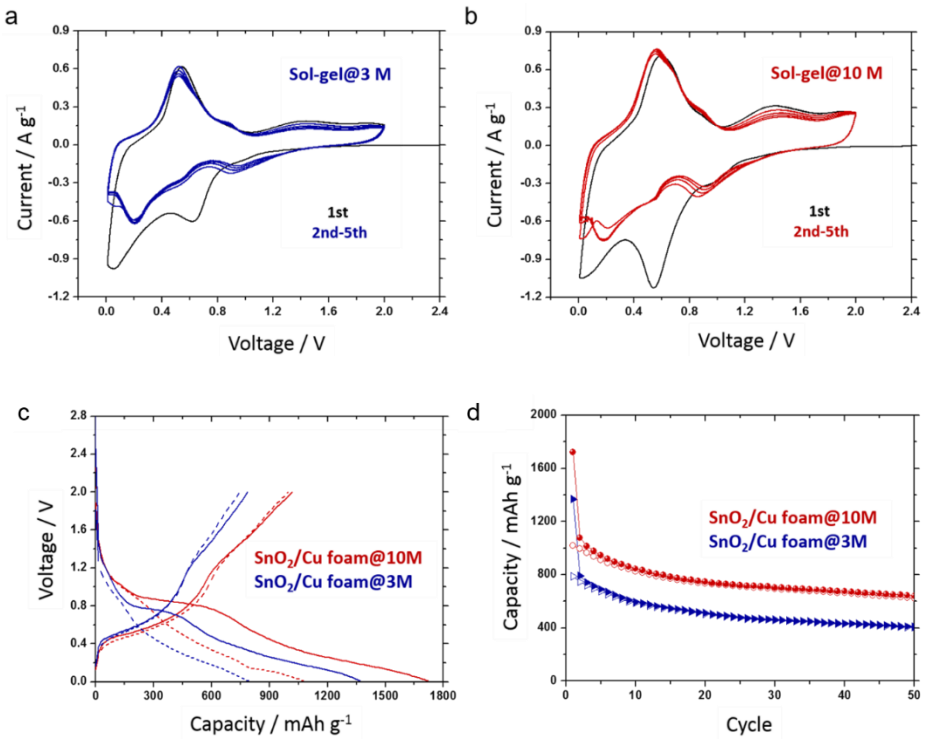


**Fig. 3.4** Cyclic voltammograms of (a) $SnO_2$/Cu foam@3M and (b) $SnO_2$/Cu foam@10M at the first five cycles at a scan rate of 0.1 mV $s^{-1}$ between 0.01 V and 2 V, (c) discharge/charge curves of $SnO_2$/Cu foam@3M and $SnO_2$/Cu foam@10M at the 1st (solid line) and 2nd (dash line) cycles at 1 C, and (d) capacity compari son of $SnO_2$/Cu foam@3M and $SnO_2$/Cu foam@10M at 1 C.

yet clear, the 10 M Sn(II) solution was used in our investigation of high capacity electrode.

The electrochemical properties of the $SnO_2$/Cu foam were further examined by introducing a commercial $SnO_2$ powder electrode which was pasted on a Cu foil and referred to as $SnO_2$ NPs, as a control group. The cycling performances of the $SnO_2$/Cu foam and $SnO_2$ NPs at 1 C between 0.01 and 2 V are presented in Fig. 3.5a. Although the capacities of both $SnO_2$/Cu foam and $SnO_2$ NPs decreased in the early cycles, the $SnO_2$/Cu foam subsequently exhibited stable capacity retention and a reversible capacity as high as 621 mAh $g^{-1}$ after 50 discharge/charge cycles. The high Li ion storage of the $SnO_2$/Cu foam is fairly comparable to that of recently reported Sn-based anode materials. Additionally, the coulombic efficiencies of the $SnO_2$/Cu foam (inset of Fig. 3.5a) remained relatively stable, whereas those of the $SnO_2$ NPs were considerably lower and fairly unstable over all of the cycles. As shown in Fig. 3.5b, the first discharge and charge capacities of the $SnO_2$/Cu foam were 1720 and 1017 mAh $g^{-1}$, respectively, and those of the $SnO_2$ NPs were 1983 and 988 mAh $g^{-1}$, respectively, which indicates that the coulombic efficiency of the $SnO_2$/Cu foam was 10% higher than that of the $SnO_2$ NPs. Additionally, the second charge capacities of the $SnO_2$/Cu foam and $SnO_2$ NPs were 998 and 938 mAh $g^{-1}$, respectively. From a comparison of the first and second charge capacities, the rate of decrease in the capacity of the $SnO_2$ NPs is approximately 2.7 times faster than that of the $SnO_2$/Cu foam. The rate capability of $SnO_2$/Cu foam cycled between 0.01 and 2 V was evaluated stepwise by increasing the C-rate from 0.1 C to 2 C

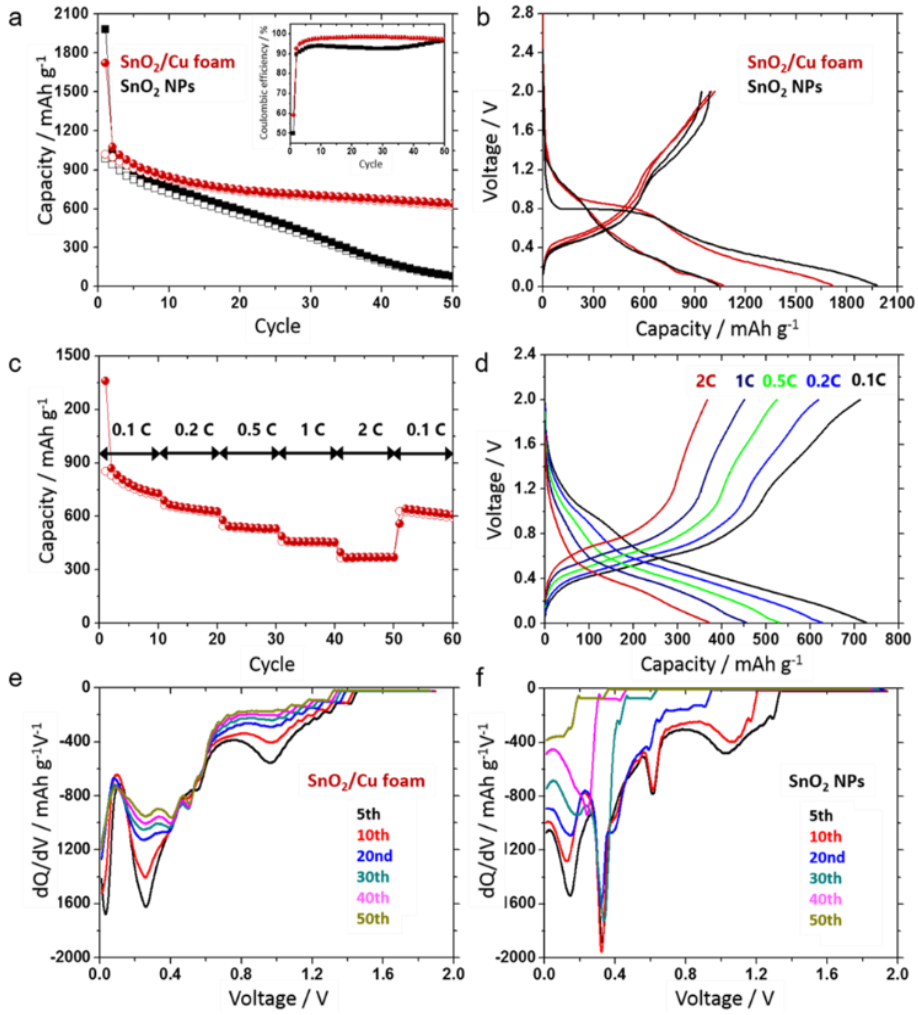


**Fig. 3.5** (a) Cycle performance of $SnO_2$/Cu foam and $SnO_2$ NPs at 1 C for 50 cycles with the inset of coulombic efficiencies, (b) voltage profiles of $SnO_2$/Cu foam and $SnO_2$ NPs during the first two cycles at 1 C, (c) capacity and (d) voltage profiles of $SnO_2$/Cu foam cycled at various rates, and (e) dQ/dV profiles of $SnO_2$/Cu foam and (f) of $SnO_2$ NPs at 1 C at selected cycle.

and then returning to 0.1 C as shown in Fig. 3.5c. When cycled at 0.1 C, the first charge capacity of 852 mAh $g^{-1}$ decreased to 713 mAh $g^{-1}$ for the subsequent 10 cycles, and then the capacity became stable as the C-rate increased. At a significantly high rate of 2 C (1562 mA $g^{-1}$), the $SnO_2$/Cu foam delivered high capacity of 368 mAh $g^{-1}$ with good stability, which is comparable with recent reports on Sn-based materials,[32,33] or even better.[34-36] When the C-rate was reduced back to 0.1 C after 50 cycles, the $SnO_2$/Cu foam recovered a respectable amount of the first 0.1 C step capacity, demonstrating its excellent rate capability. Fig. 3.5d presents the last discharge/charge voltage profiles of each rate step as shown in Fig. 3.5c. As the C-rate increased, the lithiation potential decreased and the delithiation potential increased, which is due to the kinetic effects of the material.[37] Moreover, the lithiation potential at a significantly high rate of 2 C exhibited a sloping profile between 0.01 and 0.3 V, corresponding to the formation of amorphous $Li_xSn$.[27-29,38] The differential capacity profiles (dQ/dV *vs.* voltage) of the $SnO_2$/Cu foam and $SnO_2$ NPs are shown in Figs. 3.5e and f. The distinct peaks between 0.0 and 0.7 V correspond to the lithiation steps for forming the $Li_xSn$ alloys. For the $SnO_2$/Cu foam, the intensities corresponding to the $Li_xSn$ peaks diminished with a slowly decreasing rate, and they retained a relatively large area after 50 cycles. However, the intensities of the $SnO_2$ NPs rapidly decreased and nearly disappeared at the 50th cycle, which suggests that the insertion of Li ions into the $SnO_2$ NPs no longer occurs, which is in contrast to the $SnO_2$/Cu foam. The clearly stable Li ion storage of the $SnO_2$/Cu foam may be attributed

**Table 3.1** Comparison of the electrochemical performance of Sn-based materials reported in literatures and this work.

| | Voltage range / V | Cycle | Current density / mA $g^{-1}$ | Capacity / mAh $g^{-1}$ |
|---|---|---|---|---|
| Our data | 0.01 - 2 | 50 | 781 | 621 |
| Mesoporous $TiO_2$-Sn/C Core-Shell Nanowire Arrays[39] | 0.01 - 3 | 160 | 335 | 459 |
| Three-Dimensional Porous Core-Shell Sn@Carbon Composite[15] | 0.02 - 3 | 315 | 25 | 638 |
| Tin-Core/Carbon-Sheath Coaxial Nanocables[33] | 0.005 - 2.5 | 50 | 50 | 630 |
| Graphene-Confined Sn Nanosheets[36] | 0.005 - 2 | 60 | 50 | 590 |
| 3D Nanoporous Au-Supported Nanocrystalline Tin[40] | 0.005 - 2<br>0.005 - 1 | 140 | 100 | 420<br>599 |

to its 3D interconnected structure, effectively accommodating the large volume changes of Sn with repeated lithiation/delithiation processes, and thereby preventing the pulverization of Sn particles and the loss of its electrical connection.

To certify the stabilizing effect of the $SnO_2$/Cu foam, the cells of both $SnO_2$/Cu foam and $SnO_2$ NPs after 50 cycles at 1 C were disassembled and examined as shown in Fig. 3.6a-e. The electrode morphology of the $SnO_2$/Cu foam retained its original architecture after cycling, whereas that of the $SnO_2$ NPs was quite different. In contrast to the $SnO_2$/Cu foam, the poor contact between $SnO_2$ nanoparticles and current collector in the $SnO_2$ NPs resulted in the rapid capacity fading. To further examine the surface and cross-sectional morphology of the $SnO_2$/Cu foam, the electrode after cycling was investigated using FE-SEM and FIB milling. As shown in Fig. 3.7a, the morphology of the $SnO_2$/Cu foam after cycling was similar to that before cycling (Fig. 3.1d). Moreover, the $SnO_2$ coating layer on the Cu foam was still present after 50 cycles, and its thickness increased to 480 nm, corresponding to an expansion ratio of ~153% based on a comparison of the $SnO_2$ thickness before (Fig. 3.7b) and after (Fig. 3.7c) cycling. The presence of the stable $SnO_2$ coating layer on the Cu foam without severe separation from current collector maintained the electrical connection to the Cu foam, which provided the electrode with excellent cycling performance.

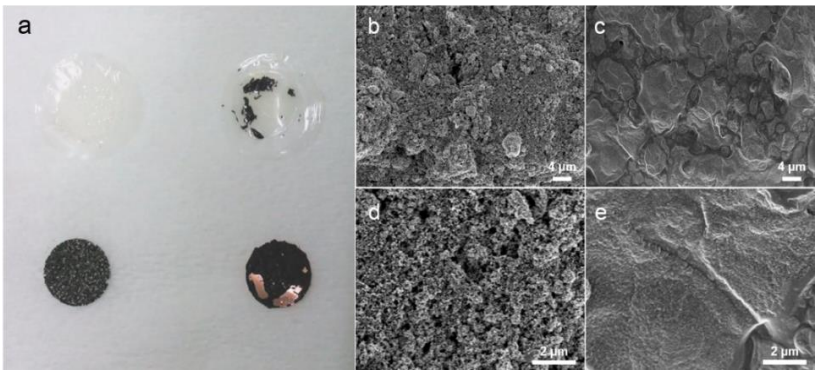


**Fig. 3.6** (a) Phtograph of disassembled electrodes and separators, SEM images of disassembled $SnO_2$ NPs electrode (b) before and (c) after 50 cycles at 1 C, (d) and (e) SEM images at high magnification of (b) and (c), respectively.

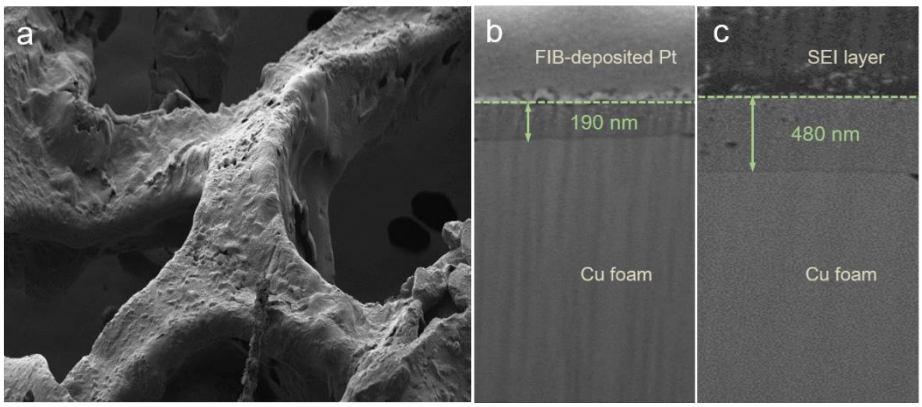


**Fig. 3.7** (a) FE-SEM image of $SnO_2$/3D foam after 50 cycles, and (b) and (c) cross-sectional image of $SnO_2$/3D foam before and after cycling, respectively.

### 3.1.4. Conclusions

A $SnO_2$-coated Cu foam was obtained through a simple sol-gel synthesis, and was electrochemically investigated as an anode for LIBs. This electrode, which was integrated with current collector and without the addition of binder and conducting agent, delivered a high reversible capacity of 621 mAh $g^{-1}$ at 1 C after 50 cycles and an excellent rate performance of 368 mAh $g^{-1}$ at 2 C. The high Li ion storage and rate capability were attributed to the 3D continuous Cu foam scaffold and the interconnected porous structure for the facile transport of electrons and Li ions. From a comparison with the conventional $SnO_2$ nanoparticle electrode, the superiority of 3D scaffold architecture, particularly for the alleviating the severe volume changes of Sn, was demonstrated by preserving its original architecture. These results indicate that the $SnO_2$/Cu foam has promising applications as a self-supporting, binder- and carbon-free anode for advanced LIBs.

## 3.2. References


1. Y. Idota, T. Kubota, A. Matsufuji, Y. Maekawa and T. Miyasaka, *Science*, 1997, **276**, 1395.

2. I. A. Courtney and J. R. Dahn, *J. Electrochem. Soc.*, 1997, **144**, 2045.

3. T. Brousse, R. Retoux, U. Herterich and D. M. Schleich, *J. Electrochem. Soc.*, 1998, **145**, 1.

4. J. S. Chen and X. W. Lou, *Small*, 2013, **9**, 1877.

5. Z. Wang, L. Zhou and X. W. Lou, *Adv. Mater.*, 2012, **24**, 1903.

6. G. Cui, Y.-S. Hu, L. Zhi, D. Wu, I. Lieberwirth, J. Maier and K. Müllen, *Small*, 2007, **3**, 2066.

7. J. R. Dahn, T. Zheng, Y. Liu and J. S. Xue, *Science*, 1995, **270**, 590.

8. R. Mukherjee, A. V. Thomas, A. Krishnamurthy and N. Koratkar, *ACS Nano*, 2012, **6**, 7867.

9. J. Liu, Y. Li, X. Huang, R. Ding, Y. Hu, J. Jiang and L. Liao, *J. Mater. Chem.*, 2009, **19**, 1859.

10. J. Ye, H. Zhang, R. Yang, X. Li and L. Qi, *Small*, 2010, **6**, 296.

11. M.-S. Park, G.-X. Wang, Y.-M. Kang, D. Wexler, S.-X. Dou and H.-K. Liu, *Angew. Chem. Int. Ed.*, 2007, **46**, 750.

12. J. Y. Huang, L. Zhong, C. M. Wang, J. P. Sullivan, W. Xu, L. Q. Zhang, S. X. Mao, N. S. Hudak, X. H. Liu, A. Subramanian, H. Fan, L. Qi, A. Kushima and J. Li, *Science*, 2010, **330**, 1515.

13. S. Ding, J. S. Chen and X. W. Lou, *Adv. Funct. Mater.*, 2011, **21**, 4120.

14. H. B. Wu, J. S. Chen, X. W. Lou and H. H. Hng, *J. Phys. Chem. C*, 2011, **115**, 24605.

15. X. Li, A. Dhanabalan, L. Gu and C. Wang, *Adv. Energy Mater.*, 2012, **2**, 238.

16. H. Zhang, X. Yu and P. V. Braun, *Nat. Nanotechnol.*, 2011, **6**, 277.

17. X. Zhu, Z. Guo, P. Zhang, G. Du, R. Zeng, Z. Chen and H. Liu, *ChemPhysChem*, 2009, **10**, 3101.

18. L. Ji, Z. Tan, T. Kuykendall, E. J. An, Y. Fu, V. Battaglia and Y. Zhang, *Energy Environ. Sci.*, 2011, **4**, 3611.

19. H. Zhang and P. V. Braun, *Nano Lett.*, 2012, **12**, 2778.

20. Y. Fu, Z. Yang, X. Li, X. Wang, D. Liu, D. Hu, L. Qiao and D. He, *J. Mater. Chem. A*, 2013, **1**, 10002.

21. W. Ni, H. B. Wu, B. Wang, R. Xu and X. W. Lou, *Small*, 2012, **8**, 3432.

22. J. Lin, Z. Peng, C. Xiang, G. Ruan, Z. Yan, D. Natelson and J. M. Tour, *ACS Nano*, 2013, **7**, 6001.

23. N. Li, C. R. Martin and B. Scrosati, *Electrochem. Solid-State Lett.*, 2000, **3**, 316.

24. J. Y. Xiang, J. P. Tu, Y. F. Yuan, X. H. Huang, Y. Zhou and L. Zhang, *Electrochem. Commun.*, 2009, **11**, 262.

25. M. Bhagwat, P. Shah and V. Ramaswamy, *Mater. Lett.*, 2003, **57**, 1604.

26. Y.-Y. Zhu, S.-R. Wang, L.-J. Zhu, X.-L. Ge, X.-B. Li and Z.-Y. Luo, *Catal. Lett.*, 2010, **135**, 275.

27. I. A. Courtney and J. R. Dahn, *J. Electrochem. Soc.*, 1997, **144**, 2045.

28. Y. Zhao, J. Li, N. Wang, C. Wu, G. Dong and L. Guan, *J. Phys. Chem. C*, 2012, **116**, 18612.

29. Y. Yang, X. Ji, F. Lu, Q. Chena and C. E. Banks, *Phys. Chem. Chem. Phys.*, 2013, **15**, 15098.

30. K. Kravchyk, L. Protesescu, M. I. Bodnarchuk, F. Krumeich, M. Yarema, M. Walter, C. Guntlin and M. V. Kovalenko, *J. Am. Chem. Soc.*, 2013, **135**, 4199.

31. R. Demir-Cakan, Y.-S. Hu, M. Antonietti, J. Maier and M.-M. Titirici, *Chem. Mater.*, 2008, **20**, 1227.

32. D. Wang, X. Li, J. Yang, J. Wang, D. Geng, R. Li, M. Cai, T.-K. Sham and X. Sun, *Phys. Chem. Chem. Phys.*, 2013, **15**, 3535.

33. B. Luo, B. Wang, M. Liang, J. Ning, X. Li and L. Zhi, *Adv. Mater.*, 2012, **24**, 1405.

34. H. Zhang, H. Song, X. Chen and J. Zhou, *J. Phys. Chem. C*, 2012, **116**, 22774.

35. C. Wang, Y. Li, Y.-S. Chui, Q.H. Wu, X. Chen and W. Zhang, *Nanoscale*, 2013, **5**, 10599.

36. B. Luo, B. Wang, X. Li, Y. Jia, M. Liang and L. Zhi, *Adv. Mater.*, 2012, **24**, 3538.

37. Y. Wu, Y. Wei, J. Wang, K. Jiang and S. Fan, *Nano Lett.*, 2013, **13**, 818.

38. H. Wu, G. Yu, L. Pan, N. Liu, M. T. McDowell, Z. Bao and Y. Cui, *Nat. Commun.*, 2014, **4**, 1943.

39. J.-Y. Liao and A. Manthiram, *Adv. Energy Mater.*, 2014, 1400403.

40. Y. Yu, L. Gu, X. Lang, C. Zhu, T. Fujita , M. Chen and J. Maier, *Adv. Mater.*, 2011, **23**, 2443.

## 3.3. Tin oxide deposited copper layer-by-layer assembly

### 3.3.1. Introduction

Developing technologies for portable electronic devices, electric vehicles, and grid-scale energy storage applications demand for high-performance lithium-ion batteries (LIBs) with high energy and high power densities and good cycling stabilities[1-4]. Tin dioxide ($SnO_2$), as a promising alternative to currently used graphitic anode for next generation LIBs, has received much attention because of its high theoretical capacity of 781 mAh $g^{-1}$, which is 2 times higher than that of the conventional graphitic anode (372 mAh $g^{-1}$)[5-7]. However, practical application of the $SnO_2$-based anode has been hindered by the inherently severe volume changes (up to 300%) during the large amounts of Li ion insertion and extraction; this can cause a pulverization of active material and a loss of electrical contact, and eventually resulting in poor capacity retention[6,8]. To resolve this issue, several strategies have been proposed, such as nanoscale electrodes[9,10], electrodes hybridized with carbon or polymers[11,12], and electrodes with unique architectures[13,14].

A three-dimensional (3D) porous metallic architecture should have several important benefits over a bulk-structured architecture, including the following: (i) facile access of electrolyte to the electrode surface, (ii) facilitated charge transfer across the interface between the electrode and electrolyte, (iii) relieved stress on the pulverization of active material by providing void spaces to absorb large volume changes, additionally, (iv) high electron pathways in the electrode assembly[15-17]. Various fabrications about the 3D

metallic scaffold have been explored such as inverse opal structure[15,18], stainless steel mesh[19], foams[20,21], long chains of particles[22], and fibers[23] or wires[24] assembly. Furthermore, a dual pore-size and pore-shape distribution architecture, interdigitated highly porous metallic scaffold, could enhance the utilization of void spaces and the volume density of active material by increasing surface area of the 3D scaffold as a template for deposited active material or as an active material itself[15,18,25,26]. In fact, many other applications such as supercapacitors[27,28], catalysts[29] or membrane electrode assembly[30] for fuel cells, and $CO_2$ capture[31] require both smaller pores for large effective surface area and efficient chemical activity and larger pores for effective mass transport and efficient reaction kinetics when liquids, solids, and gases are involved in reactions[32].

To achieve the above dual pore architecture, a freeze-casting process could be employed. This process is an easy, versatile, and promising method to prepare a highly interconnected microscale pore structure[33-37]. In this low-cost, robust, and scalable process, a solution is frozen and the frozen solvent is then removed by freeze-drying, forming a porous body structure (which can be further sintered) as a replica of the solidified solvent structure[33,34]. It is also possible to control pore size, pore geometry, and porosity of the structure by properly controlling the slurry formulation, the solvent, and the solidification conditions[35-37]. As it is a physical process without chemical reactions, and as it uses ice crystals obtained from water or other forms of liquid template, freeze-casting generally results in pores on the order of tens of micrometers in size.

Herein, I report a new $SnO_2$ anode design concept, for the first time, based on a 3D porous Cu scaffold with a dual pore-size distribution by a directional freeze-casting technique. The Cu scaffold is utilized as an anode current collector concurrently with a template for a $SnO_2$ coating. The 3D porous Cu scaffold provides both continuous metallic struts to act as effective electron pathways and local void spaces to alleviate stress generated from large volume changes during cycling. This combination of properties in the electrode demonstrates remarkably high reversible capacity, excellent rate capability, and stable cycle retention with preserving its structural integrity.

### 3.3.2. Experimental section

#### 3.3.2.1. Synthesis of Cu scaffold via freeze-casting

Nano-sized cupric oxide (CuO) powder, with a particle size of 40–80 nm and 99.9% purity, was purchased from Inframat Advanced Materials (Manchester, CT., USA). Cupric oxide powder slurry was prepared through the following steps: First, 49.4 wt.% cupric oxide powder and 2.5 wt.% polyvinyl alcohol (PVA, Sigma-Aldrich Co., USA) binder were slowly suspended and dissolved in 30 ml deionized water, respectively, by using stirring and sonication. The slurry was then cooled to a few degrees above the freezing point of water and poured into a Teflon mold (54 mm in interior diameter, 77 mm in length) placed on a copper rod. The freeze-casting apparatus is shown schematically in Fig. 3.8. The insulated steel container was filled with liquid nitrogen (outer) and ethyl alcohol (interior) and the temperature at the top of the copper rod was fixed at -10 ℃ using a heater. During directional freezing of the cupric oxide slurry, growth of vertical ice crystal colonies occurred, accompanied by entrapment of copper oxide particles between the ice crystals[35,36]. Once freezing was completed, the sample underwent sublimation in a freeze dryer for 40 h at -88 °C under 0.005 torr vacuum. After sublimation of the ice, a continuous, porous, layered-structure resulted, consisting of elongated channels separated by interconnected, parallel walls consisting of lightly-bound copper oxide particles. The green-body foam was then reduced from copper oxide to copper in a hydrogen atmosphere. Reduction and sintering consisted of presintering at

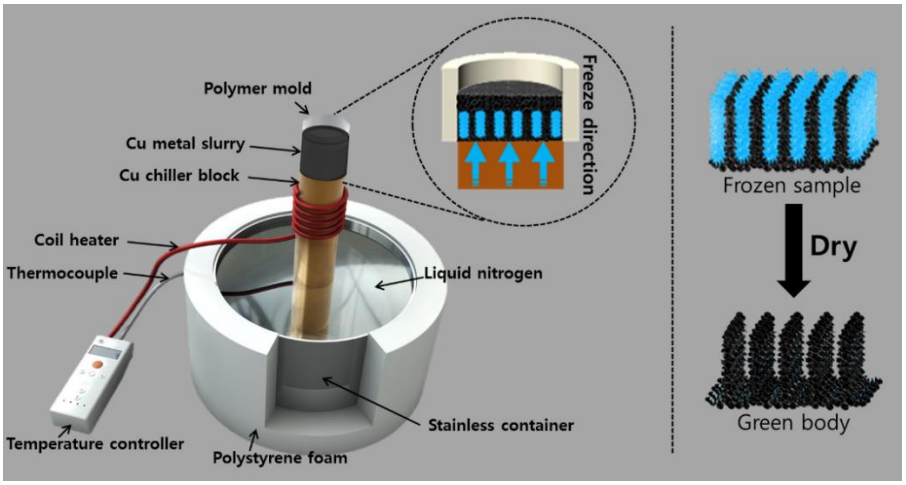


**Fig. 3.8** Schematic diagram of the freeze-casting apparatus.

250 °C for 4 h and primary sintering at 800 °C for 14 h; these were conducted in a tube furnace containing a 5% $H_2$/Ar gas atmosphere at a heating rate of 5 °C $min^{-1}$. As shown in Fig. 3.9a the dark green copper oxide foam turned to a typical Cu orange after reduction in the hydrogen atmosphere and underwent a volume shrinkage of 44 %.

### 3.3.2.2. Deposition of $SnO_2$ through a sol-gel process

Prior to applying the $SnO_2$ coating to the freeze-cast copper scaffold, the Cu scaffold samples were cut into thin coupons and polished to 300 μm thickness with colloidal alumina following standard metallographic procedures. Finally, disks 11 mm in diameter were then punched out (Fig. 3.9a). The prepared Cu scaffold coupons were heated at 500 °C for 1 h in a 5% $H_2$/Ar mixture gas to burn off any remaining binder or leftover solution from the polishing process and to remove the surface oxide layer on the Cu scaffold. A $SnO_2$-based solution was prepared by dissolving 0.338 g of $SnCl_2 \cdot 2H_2O$ in a solvent mixture consisting of 0.03 mL 37% hydrochloric acid and 0.47 mL ethanol to obtain a 3 M Sn(II) solution (0.564 and 1.128 g of $SnCl_2 \cdot 2H_2O$ for 5 and 10 M, respectively), which was subsequently aged at room temperature for 24 h. Triple deionized water (DI-$H_2O$) was then added to the solution, which was aged for another 24 h. The copper foam coupons were immersed in the prepared gel for 24 h, followed by solvent evaporation at 80 °C in vacuum. Heat treatment at 500 °C in an Ar atmosphere for 2 h converted the tin oxide precursor gel into crystalline $SnO_2$ (Fig. 3.9b)[38,39]. The weight of coated $SnO_2$ as

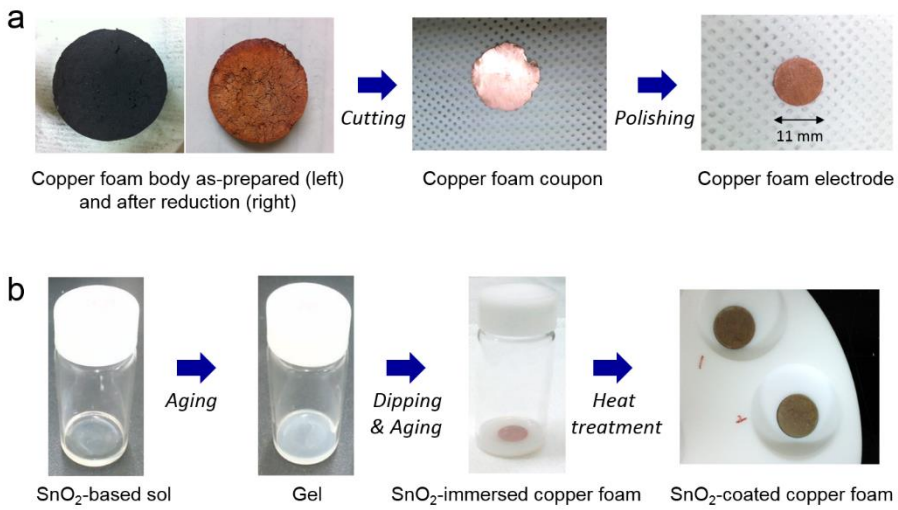


**Fig. 3.9** Photographs of (a) Cu scaffold preparation and (b) sol-gel coating process.

an active material in each $SnO_2$@Cu scaffold electrode was measured to five decimal place in an electronic scale by weight difference between the pristine Cu foam after $H_2$/Ar pre-heat treatment and the $SnO_2$-coated Cu scaffold after sol-gel method.

### 3.3.2.3. Electrochemical Measurements

The $SnO_2$@Cu scaffold, without the addition of any binder or conductive agent, was assembled into a coin cell to be used as a working electrode, and was compared with a $SnO_2$ powder electrode as control. For the control $SnO_2$ powder electrode, commercial $SnO_2$ NPs (<100 nm, purchased from Aldrich) was mixed with Ketchen Black as a conductive agent, and PVDF as a binder, in N-methyl-2-pyrrolidone (NMP) solvent. The $SnO_2$: Ketchen Black: PVDF weight ratio was 80:10:10. The mixed slurry was uniformly pasted using a doctor blade method onto a Cu foil 20 μm in thickness to serve as a conventional current collector. The electrodes were dried under vacuum at 120 °C for 8 h and then pressed at room temperature. 2032-type coin cells, consisting of $SnO_2$@Cu scaffold or $SnO_2$ NPs as the working electrode and with a lithium metal foil as both the counter and reference electrodes, were assembled in a glove box under a dry Ar atmosphere. The electrolyte used in this study was 1.0 M $LiPF_6$ dissolved in a mixture of ethylene carbonate (EC) and diethyl carbonate (DEC) in a volume ratio of 1:1. Galvanostatic tests (WBCS3000 cycler, WonATech, Korea) were carried out on the coin cells at a current rate of 1 C (781 mA $g^{-1}$) in the voltage range of 2.0 V to 0.01 V (*vs.* $Li^+$/Li)

at 25 °C.

### 3.3.2.4. Characterization

XRD patterns were obtained with a Bruker D-5005 using Cu Kα radiation (λ = 1.5406 Å ), operating at 40 kV and 40 mA with a scan range of 20–80°. The morphologies of specimens were characterized using field emission scanning electron microscopy (FE-SEM), (Carl Zeiss, SUPRA 55VP). Pore size distribution and porosity measurements were analyzed for the Cu foam using Hg intrusion porosimetry (MIP), (AutoPore IV 9510, Micromeritics). X-ray photoelectron spectrometer (XPS) was operated on the surface of electrode with Ar ion beam etching during 240 sec using VG Scientifics (Al Kα source). The results were calibrated by referencing C1s at 285 eV using Avantage software. Electrochemical impedance spectroscopy (EIS) was conducted with open-circuit voltage in 10 mV amplitude with the frequency range from 100 kHz to 10 mHz (Zahner, Germany).

### 3.3.3. Results and discussion

#### 3.3.3.1. Material and structure design

The freeze-casting technique was initially invented for use with porous ceramics and polymers because of their lower densities and the ease of suspension of particles in slurries. Since the first report on the use of biomedical materials obtained from collagen solutions by Schoof *et al.* in 1998[40], the viability of freeze-casting for ceramic-based porous biomaterials has been widely investigated. In contrast, freeze-cast metals were not created until recently due to difficulties with particle settling in, and reactivity with, the solvent. Such foams were fabricated through freeze-casting using titanium powders[41], copper oxide powders[42] and iron oxide powders[43] (which were reduced to copper and iron, respectively). Among the prepared metal (Ti, Cu, and Fe) foams, the Cu foam was regarded as the best scaffold as a current collector because of the highest electrical conductivity. Moreover, the unique dual pore structure formed in directionally freeze-cast Cu foams is of particular interest for electrodes. The channel-like, elongated pores created by templating of ice dendrites, separated by sintered Cu walls, are several tens of micrometers in width, whereas the much smaller pores templated on one side of the Cu foam wall surface by secondary dendrite arms have dimensions on the order of several micrometers.

As a further step, $SnO_2$ as an active material should be combined with the Cu scaffold current collector to react with Li ions. For advanced Sn-based materials, various synthesis

methods have been developed such as sputtering, chemical vapor deposition, and electron beam deposition and so on. However, these methods have low throughput and require vacuum conditions, making economical scale-up difficult. One alternative approach is to use a sol-gel method, which has many advantages over the conventional methods using solid-state reactions. For instance, the sol-gel method can provide good stoichiometric control, homogeneous molecular or atomic mixing, uniform particle size distribution, and small particle size, even down to the nanometer level[44]; in addition, it does not require a vacuum system and is thus scalable at low cost. We therefore chose to utilize a sol-gel method[43,44] to apply a $SnO_2$ coating to the Cu scaffold current collector. The fabrication processes of Cu foam via directional freeze-casting and $SnO_2$ coating via sol-gel are schematically illustrated in Fig. 3.10. One can thus fabricate a $SnO_2$-coated Cu foam (hereafter, referred to as $SnO_2$@Cu scaffold) anode by integrating three simple processes: freeze-casting/drying, reduction/sintering, and sol-gel coating, which can be linked into a single, continuous process that is able to scale up to very high throughput. In addition, the choice of active coating material does not need to be confined to $SnO_2$, but is open to other active materials, as is the choice of Cu for the current collector.

#### 3.3.3.2. Preparation of $SnO_2$-coated Cu scaffold electrode

FE-SEM images (Fig. 3.11a-g) show morphologies of an as-prepared Cu scaffold prior to application of the $SnO_2$ coating. The Cu scaffold presents the various morphological

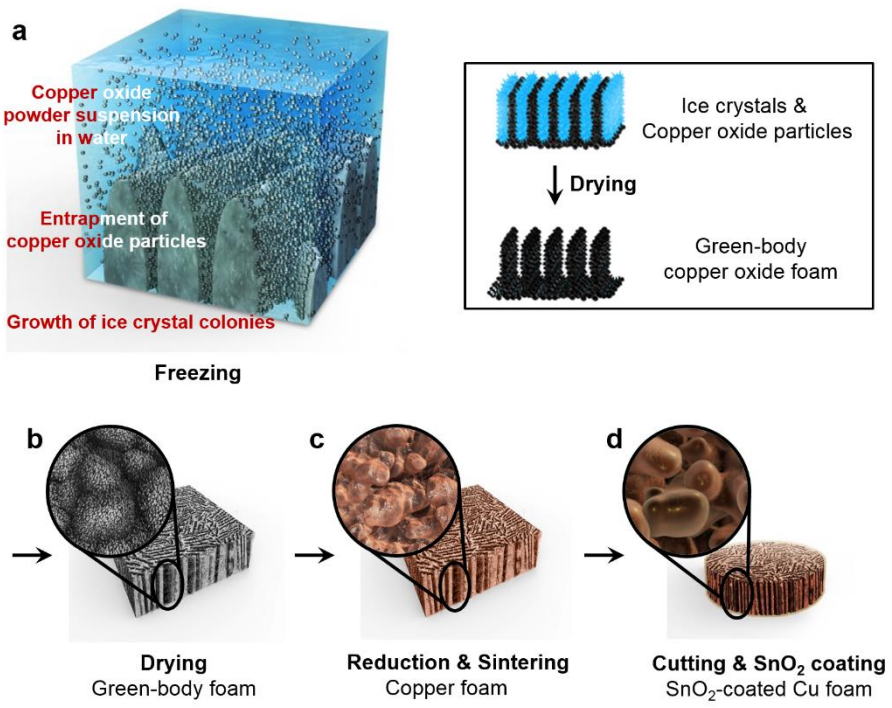


**Fig. 3.10** Schematic fabrication steps for a $SnO_2$-coated Cu scaffold electrode.

characteristics upon comparing side views (Fig. 3.11b-d) with top views (Fig. 3.11e-g). First, Fig. 3.11a shows a layered lamellar assembly of Cu walls or lamellae. Second, the magnified surface morphology on a lamella (Fig. 3.11c,d) shows a high degree of roughness caused by dendritic-like morphologies of the ice crystals[35,36], and confirms the presence of numerous small pores ca. 10 μm in diameter. Third, the dendritic features appear on the surface of lamellae. The top images of Cu scaffold in Fig. 3.11a,b also exhibit a randomly oriented layered structure perpendicular to the ice front. Although the lamella thicknesses and the intervals between lamellae (Fig. 3.11e) vary considerably, they are estimated to be 50 and 100 μm, respectively. Fig. 3.11g displays the development of dendrites in side view, which is also observed from Fig. 3.11d in front view. Moreover, the corresponding cross-sectional optical images of as-prepared Cu scaffold are shown in vertical and horizontal views (Fig. 3.12a and b, respectively), revealing numerous, continuous, porous walls several tens of microns in width.

To evaluate the pore-size and distribution for as-prepared Cu scaffold, a mercury intrusion porosimetry (MIP) test was carried out. Because the MIP test could not detect the main channel-like pores of several hundred microns in size, those secondary pores on the order of a few tens of microns were detected. The major peak of the pore distribution was 14 μm, as seen in Fig. 3.13a, in qualitative agreement with the image in Fig. 3.11d; these pores resulted from the secondary dendritic growth of ice crystals. The inset i mages of Fig. 3.13a also show the cross-sectional area of Cu scaffold and its

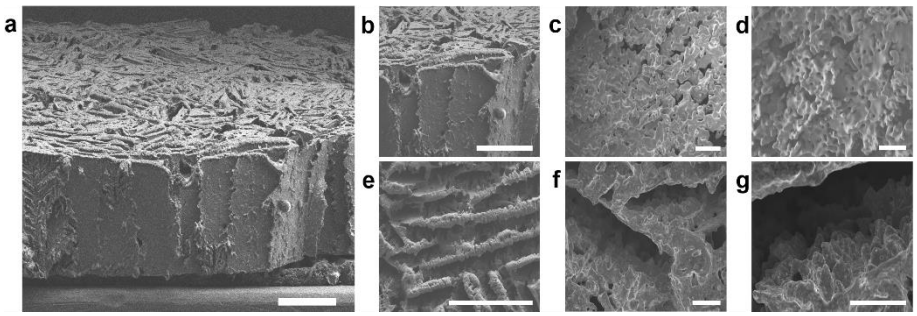


**Fig. 3.11** (a) freeze-cast Cu scaffold showing layered Cu walls replicated during the dendritic slurry casting; scale bar, 400 μm. (b-d) side view of micro-porous surface of a Cu wall; scale bars, 400 μm, 40 μm, 40 μm, respectively. (e-g) top view of Cu walls; scale bars, 400 μm, 40 μm, 40 μm, respectively. Schematic of fabrication steps for a $SnO_2$-coated Cu scaffold electrode.

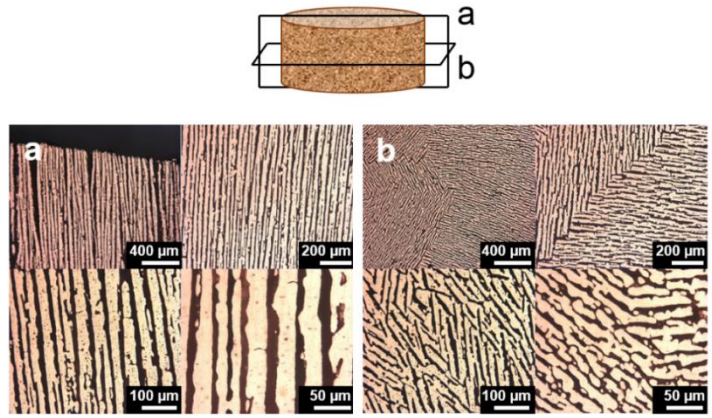


**Fig. 3.12** Optical micrographs of a polished Cu scaffold electrode, after being cut either (a) vertically or (b) horizontally.

magnified surface morphology, confirming the existence of dendritic ice crystals. The XRD pattern (Fig. 3.13b) of as-prepared Cu scaffold identifies diffraction peaks for both $Cu_2O$ and Cu; these are indexed as space groups Pn3m (JCPDS 05-0667) and Fm3m (JCPDS 04-0836), respectively. Previous findings[45,46] suggest that the surface of metallic copper exposed to air is oxidized continuously, even at room temperature, because the development of a native oxide layer on the copper surface is not a self-protective process. Moreover, surface oxidation might have also occurred during the sample polishing process. To investigate the purity of the Cu foam sample, heat treatment was carried out at 500 ºC in an Ar atmosphere or a $H_2$/Ar gas mixture, and the XRD traces compared. $Cu_2O$ still remained in the sample after being heat-treated in the Ar atmosphere, whereas no copper oxide peak was observed for treatment in the $H_2$/Ar gas mixture. This is because a continuous reduction process could occur during heat-treatment in a $H_2$/Ar gas mixture, removing Cu oxide layers from the surface of the Cu scaffold.

Fig. 3.14a shows the cross-sectional images of $SnO_2$@Cu scaffold taken by focused ion beam (FIB) milling and EDX mapping analysis, and confirms the presence of a $SnO_2$ coating after sol-gel process. The regions of interest, which are indicated by white rectangles in Fig. 3.14a, were randomly selected for comparison of the top and interior areas of the $SnO_2$@Cu scaffold. A $SnO_2$ layer at the top was coated onto the Cu scaffold and estimated to be ca. 500 nm in thickness. Moreover, the presence of an interior $SnO_2$ coating layer is clearly illustrated, as indicated by an arrow, surrounding a pore in the Cu

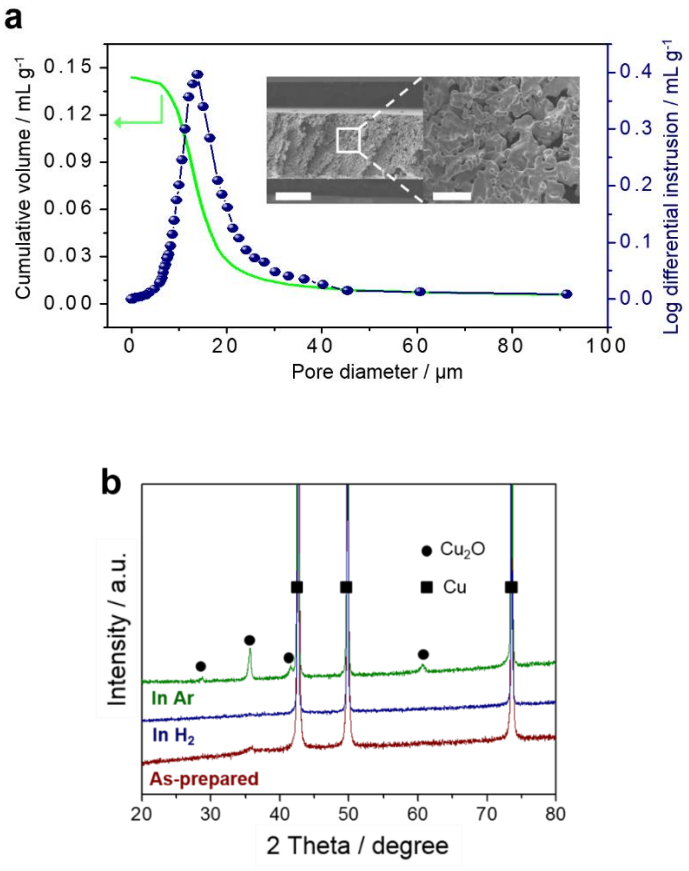


**Fig. 3.13** (a) Pore size distribution of Cu scaffold determined by MIP and (inset) cross-section SEM images of Cu scaffold; scale bars, 400 µm and 40 µm and (b) XRD patterns of as-prepared Cu scaffold (red), and of Cu scaffold after: heat treatment at 500°C in an Ar (green) or a $H_2$/Ar (blue) gas mixture atmosphere.

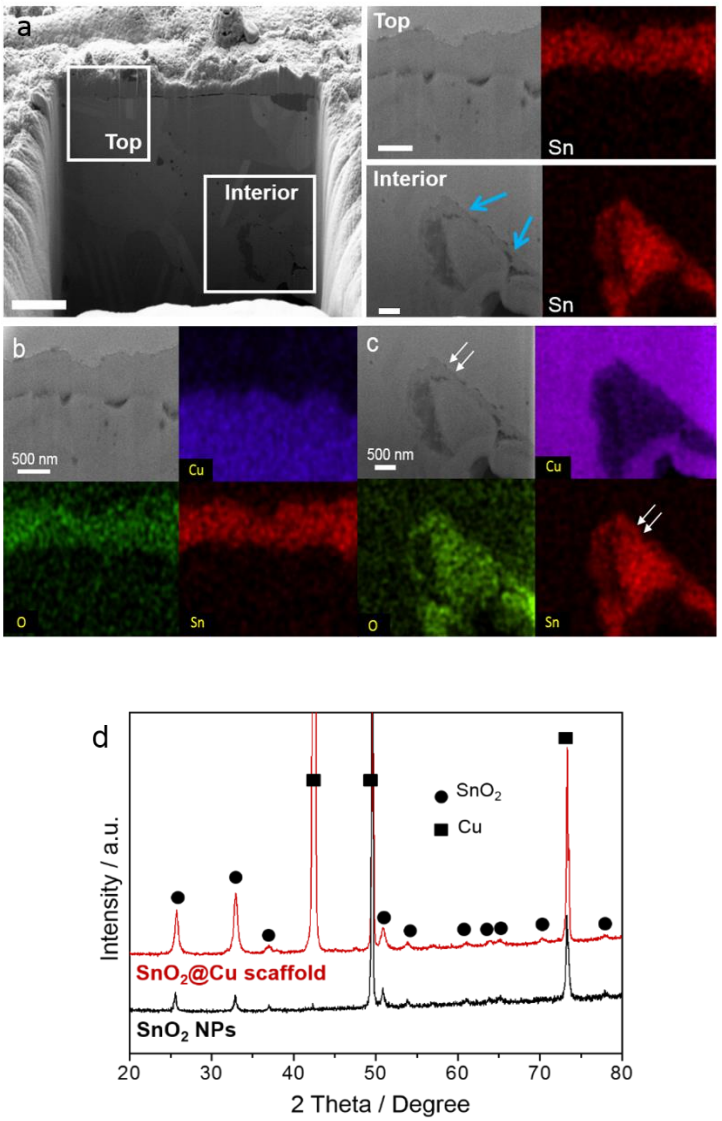


**Fig. 3.14** SEM and EDX images of (a) surface and cross-sections of electrode, (b) top and (c) interior regions of $SnO_2$@Cu scaffold after FIB milling with Sn EDX map; scale bars, 2 μm, 500 nm, 500 nm, respectively, and (d) XRD patterns of $SnO_2$@Cu scaffold and $SnO_2$ NPs.

scaffold arising from the dendrite formation on the lamella surface. The interior $SnO_2$ coating layer is thinner than the top $SnO_2$ coating layer. Fig. 3.14d compares the XRD patterns of the $SnO_2$@Cu scaffold and commercial $SnO_2$ powder slurry pasted onto copper foil as control [hereafter, referred to as $SnO_2$ NPs (<100 nm)]. The diffraction peaks observed for both $SnO_2$@Cu scaffold and $SnO_2$ NPs were assigned to either tetragonal rutile-structure $SnO_2$ (JCPDS 41-1445) or metallic copper (JCPDS 04-0836), with no additional peaks corresponding to other phases such as SnO and $Cu_2O$.

To confirm the presence of a $SnO_2$ coating in the middle of the 300 μm thick $SnO_2$@Cu scaffold, SEM and EDX mapping images were taken at ca. 150 μm depth position. Fig. 3.15a presents an entire cross-section of the $SnO_2$@Cu scaffold sample mounted in polymer resin and polished according to standard metallographic procedures. The magnified surface on the lamella in the $SnO_2$@Cu scaffold interior (Fig. 3.15c) is covered with a bright thin layer, implying the presence of the Sn at ca. 150 μm depth (Fig. 3.15c and d). It was also observed that lamellar bridges originating from overgrown dendrites eventually crossed the gaps between two adjacent lamellae[33,36]; an example is indicated by blue rectangles in Fig. 3.15a. This observation suggests that the layer-by-layer porous structure grown in the vertical direction could make connections continuously in the horizontal direction, resulting in a well-constructed three-dimensional Cu network structure.

XPS depth profiles with Ar ion beam etching were used to further probe the chemical

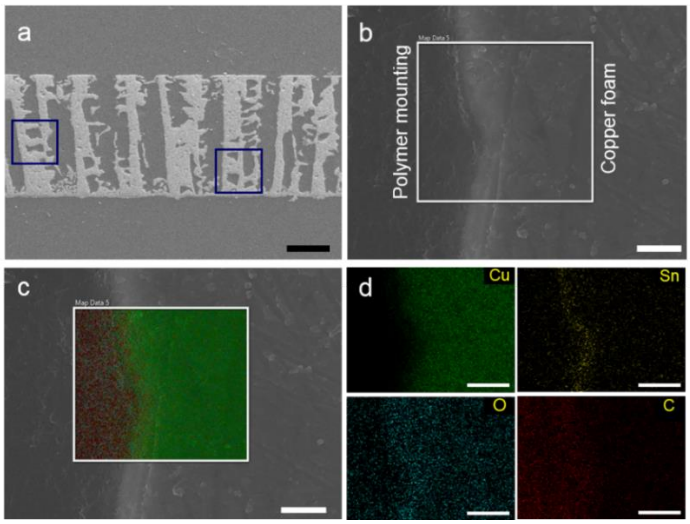


**Fig. 3.15** EDX mapping images of a cross-section of $SnO_2$@Cu scaffold showing $SnO_2$ coating in the middle of the 300 μm thick $SnO_2$@Cu scaffold.

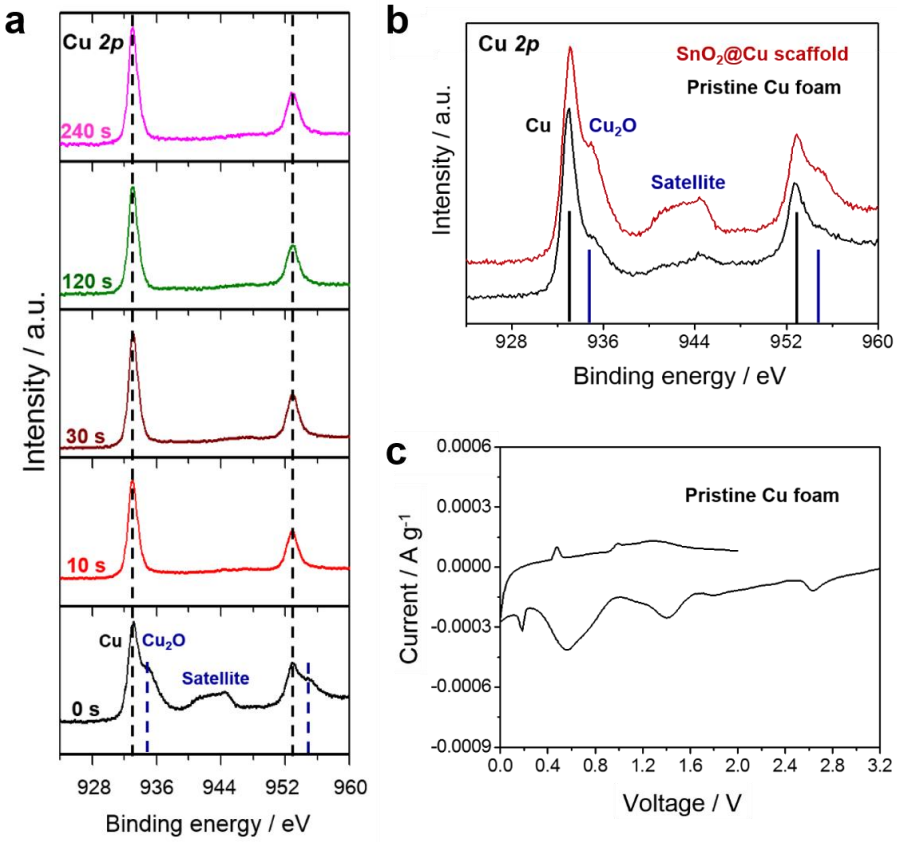


**Fig. 3.16** (a) XPS profiles of $SnO_2$@Cu scaffold with various Ar ion etching time, (b) Comparison of oxidation state of pristine Cu foam and $SnO_2$@Cu scaffold, and (c) Cyclic voltammogram of pristine Cu foam at a scan rate of 0.1 mV/s.

oxidation state of the $SnO_2$@Cu scaffold (Fig. 3.16a). Metallic Cu, $Cu_2O$, and satellite peaks of $Cu^{2+}$ in CuO or probably $Cu(OH)_2$[47,48] were observed at surface of the $SnO_2$@Cu scaffold corresponding to 0 s etching time. Also, the depth profiles from 10 s to 240 s exhibit that inner Cu foam preserves the metallic Cu state after $SnO_2$ coating. The $Cu_2O$, not observed in XRD pattern (Fig. 3.14d), was also observed in the pristine Cu foam (Fig. 3.16b), after $H_2$/Ar gas heat treatment and prior to $SnO_2$ coating, which implies that traces of Cu foam were spontaneously oxidized[45,46]. The existence of $Cu_2O$ can cause an additional specific capacity because the $Cu_2O$ reacts with Li ions (theoretical capacity of 375 mAh $g^{-1}$)[49,50]. However, the reactivity with Li ions of $Cu_2O$, formed not artificially but spontaneously, was negligible as shown in cyclic voltammetry (CV) curve; a voltage range of 0.01 V-2.0 V and a scan rate of 0.1 mV $s^{-1}$ were used (Fig. 3.16c).

#### 3.3.3.3. Electrochemical performance

The effect of $SnO_2$ sol-gel concentration in the coating process on the LIBs performance was examined. We measured the capacity for different $SnO_2$ sol-gel concentrations using current rate of 1 C. Capacity increased with increasing the sol-gel concentration as presented in Fig. 3.17. As a result, $SnO_2$ sol-gel concentration was controlled at 10 M for subsequent experiments.

CV was carried out to understand and compare the reactive process of $SnO_2$@Cu scaffold and $SnO_2$ NPs (Fig. 3.18). The behaviors of the first three CV curves of $SnO_2$@

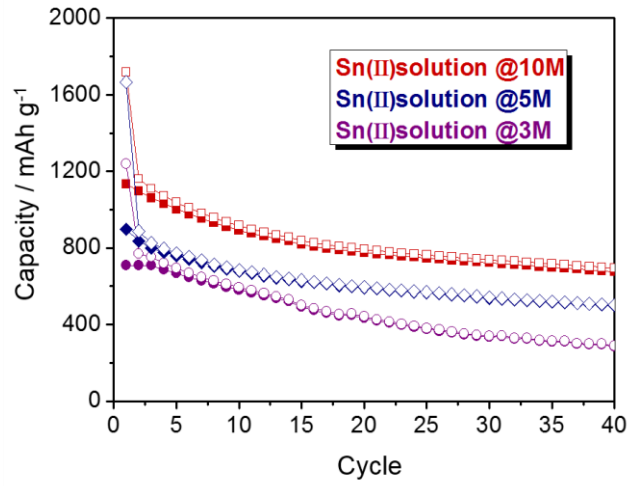


**Fig. 3.17** Capacity comparison of $SnO_2$@Cu scaffold, using sol-gel concentrations of 3 M, 5 M, and 10 M. Capacity was measured at a current rate of 1 C during 50 cycles.

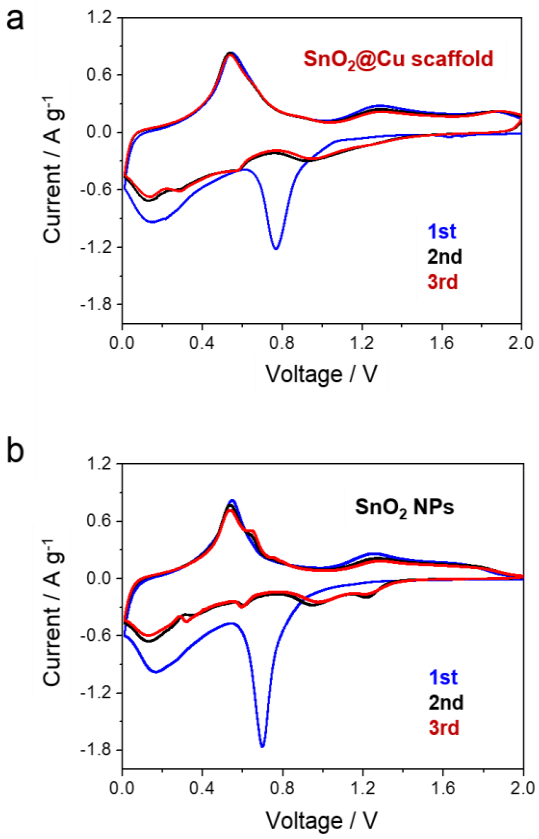


**Fig. 3.18** Cyclic voltammograms of (a) $SnO_2$@Cu foam and (b) $SnO_2$ NPs at a scan rate of 0.1 mV/s.

Cu scaffold and $SnO_2$ NPs are in accordance with the electrochemical behavior of $SnO_2$-based anode materials[51-53]. The first cathodic peak of $SnO_2$ to Sn as described by Eqs (1) and (2), respectively.

$$Li^+ + e^- + \text{electrolyte} \rightarrow \text{SEI (Li)} \quad (1)$$

$$SnO_2 + 4Li^+ + 4e^- \rightarrow Sn + 2Li_2O \quad (2)$$

$$Sn + xLi^+ + xe^- \leftrightarrow Li_xSn \quad (0 < x \leq 4.4) \quad (3)$$

This cathodic peak shifted to higher voltages around 0.92 V with broad bands in subsequent cycles, and the corresponding anodic peak appearing at 1.27 V is attributed to oxidation of Sn to $SnO_2$, suggesting the partially reversible electrochemical reaction described by Eq (2)[52,53]. Moreover, the cathodic peaks in the region of 0.0–0.7 V are due to the formation of $Li_xSn$ alloys as described by Eq (3), whereas the corresponding anodic peaks in 0.4–1.0 V are due to the Li ion extraction from those $Li_xSn$ alloys[51,54]. There was no significant changes of the anodic peaks at 0.4–1.0 V for $SnO_2$@Cu scaffold from the first to third cycles, whereas the magnitude of the anodic peaks of $SnO_2$ NPs decreased in the initial three cycles, demonstrating the enhanced cycling stability of $SnO_2$@Cu scaffold over that of $SnO_2$ NPs.

Li ion capacities of $SnO_2$@Cu scaffold and $SnO_2$ NPs at 0.5 C are shown in Fig. 3.19a; the inset plot shows coulombic efficiencies. The capacity of $SnO_2$@Cu scaffold exhibited a relatively stable reversible capacity of 750 mAh $g^{-1}$ after 50 cycles, which is better than all but one[55] of Sn-based anode reported recently[56-61]. In contrast, the capacity of $SnO_2$

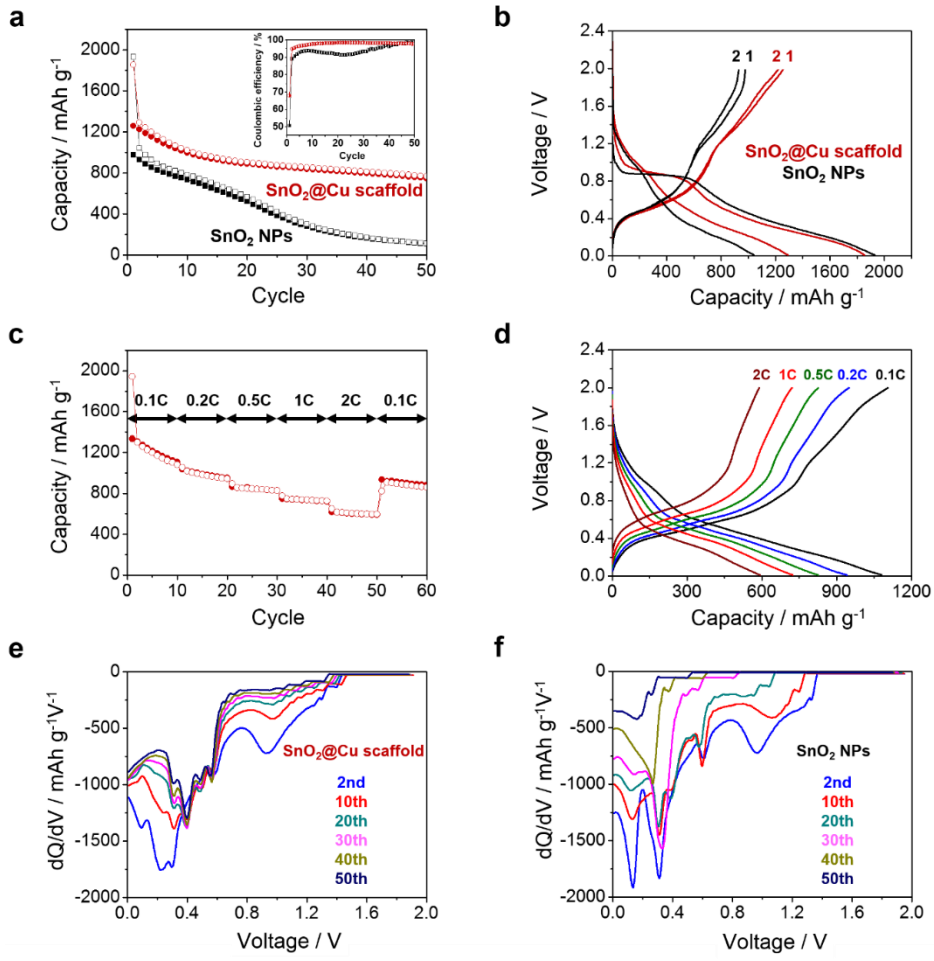


**Fig. 3.19** (a) Cycle performance of $SnO_2$@Cu scaffold and $SnO_2$ NPs at a current rate of 0.5 C for 50 cycles and (inset) their coulombic efficiencies. (b) Voltage profiles of $SnO_2$@Cu scaffold and $SnO_2$ NPs after 1st and 2nd cycles at 0.5 C. (c) Capacity and (d) voltage profiles of $SnO_2$@Cu scaffold cycled at various current densities. dQ/dV profiles of (e) $SnO_2$@Cu scaffold and (f) $SnO_2$ NPs, at a 1 C, at selected cycle numbers. All the specific capacities and current rate are calculated based on the mass of $SnO_2$.

NPs degraded by 90% during cycling. The inset of Fig. 3.19a showed that the coulombic efficiencies of $SnO_2$@Cu scaffold were high and essentially stable, whereas that of $SnO_2$ NPs were lower than that of $SnO_2$@Cu scaffold over the entire cycle range and much less stable. Fig. 3.19b shows the galvanostatic discharge/charge voltage profiles of $SnO_2$@Cu scaffold and $SnO_2$ NPs at 0.5 C. During the first cycle, the discharge curve had a plateau at around 0.8 V for both $SnO_2$@Cu scaffold and $SnO_2$ NPs, due to the formation of an SEI layer, and the conversion reaction of $SnO_2$ into Sn and $Li_2O$. The second discharge curve differed from the first in that the voltage plateau disappeared, suggesting that the formation of an SEI layer and $Li_2O$ occurred mainly in the first cycle[51,53]. This observation is consistent with the CV curves (Fig. 3.18). The rate capability of $SnO_2$@Cu scaffold was evaluated by increasing the galvanostatic current rate from 0.1 to 2 C stepwise and then decreasing back to 0.1 C, as shown in Fig. 3.19c. When cycled at 0.1 C, the initial charge capacity of 1330 mAh $g^{-1}$ decreased gradually down to 1110 mAh $g^{-1}$ by the 10th cycle. However, the capacity began to show stable capacity retention and exhibited excellent cycling stability up to the 50th cycle, where the capacity was approximately 590 mAh $g^{-1}$ at 2 C; this is a much better performance than in other recent reports also using a three-dimensional architecture[20,59-62]. After 50 cycles, when the current rate had been returned to 0.1 C, the capacity of $SnO_2$@Cu scaffold had almost recovered, showing a good rate capability. Fig. 3.20 compares the rate capabilities among a number of different Sn-based anode materials studied in recent years. This comparison confirms that the rate

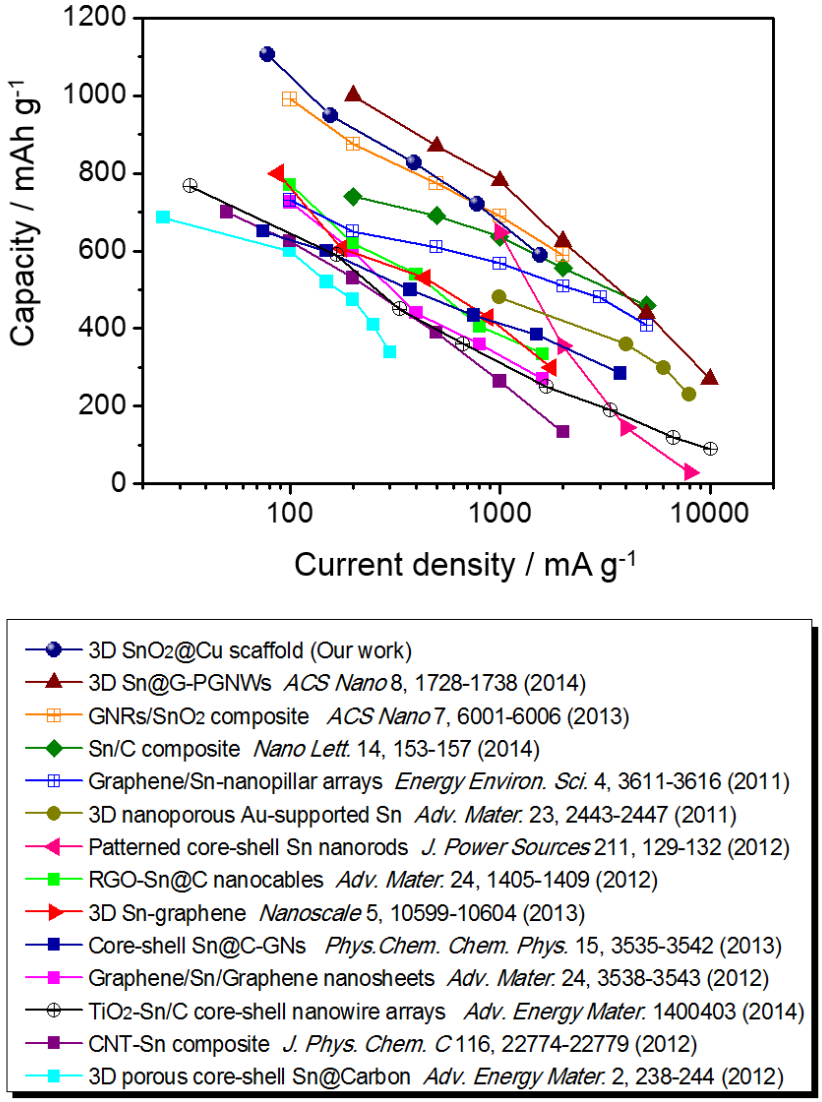


**Fig. 3.20** Comparison of capacity of $SnO_2$@Cu scaffold to other Sn-based materials recently reported in the literature.

capability of the $SnO_2$@Cu scaffold examined in this study is superior to all but the best Sn electrode reported to date[55]. Fig. 3.19d exhibits the final discharge and charge voltage profile in each current rate step, for the measurements presented in Fig. 3.19c. Even at the highest current rate of 2 C, lithiation is still observed as shown by a sloping voltage profile around 0.1 V, corresponding to the formation of $Li_xSn$[7,53]. The differential capacity *vs.* voltage plots of $SnO_2$@Cu scaffold and $SnO_2$ NPs are shown in Fig. 3.19e and f. The distinct peaks between 0.7 and 0.01 V after the second cycle correspond tothe specific lithiation steps in forming $Li_xSn$[63,64]. The lithiation peaks of $SnO_2$@Cu scaffold exhibit relatively stable behaviors after the 20th cycle, whereas those of $SnO_2$ NPs degrade and disappear at the 50th cycle, suggesting that the reversible Li ion insertion into $SnO_2$@Cu scaffold could continue. In order to reconfirm the reversible Li ion insertion for $SnO_2$@Cu scaffold in the latter part of the cyclic performance test, the 40th discharge curves of $SnO_2$ @Cu scaffold and $SnO_2$ NPs were selected and compared as shown in Fig. 3.21a. Based on the low-cycle CV curves (Fig. 3.18), the 40th discharge curve could be divided into two different voltage ranges of 0.01–0.7 V ($\Delta C_1$) and 0.7–2.0 V ($\Delta C_2$), corresponding to the formation of $Li_xSn$ alloys and $Li_2O$, respectively[52,65]. Moreover, the difference in capacities between the $SnO_2$@Cu scaffold and $SnO_2$ NPs at the 40th cycle in the respective voltage ranges was calculated and shown in Fig. 3.21b. Out of the total capacity increment of ca. 450 mAh $g^{-1}$, $\Delta C_1$ constituted 77% of the entire increment. This suggests that the reversible Li ion insertion was considerably higher with the $SnO_2$@Cu

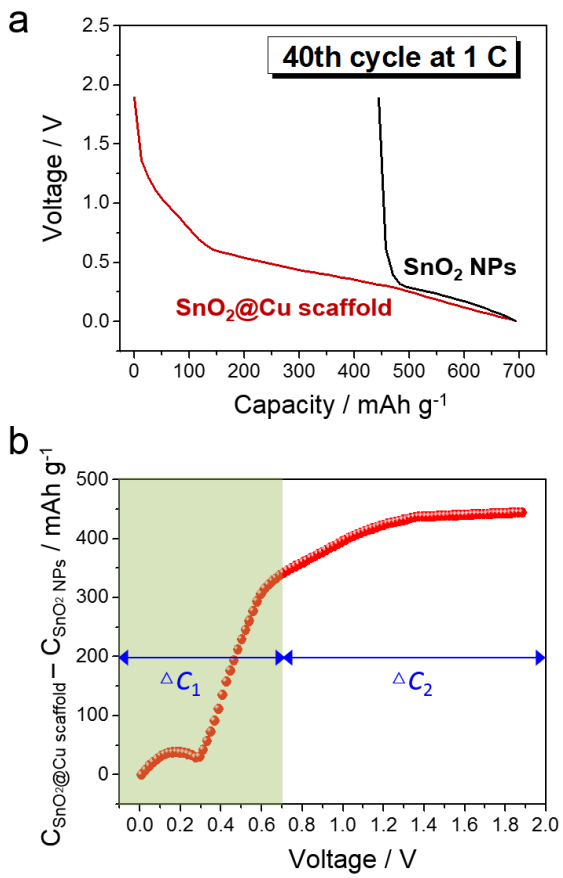


**Fig. 3.21** (a) 40th discharge voltage profiles of $SnO_2$@Cu foam and $SnO_2$ NPs at 1 C. (b) The difference between the capacities of $SnO_2$@Cu foam and $SnO_2$ NPs, at the 40th cycle.

scaffold than with the $SnO_2$ NPs. The considerable capacity increment of the $SnO_2$@Cu scaffold is attributed to its reversible alloying reaction of $Li_xSn$.

The stable cycling performance of $SnO_2$-coated Cu scaffold is ascribed to the unique 3D porous architecture with the following advantageous features: (i) the intrinsic structural integrity of the 3D open network with interconnected pores and continuous metallic walls within the electrode enables faster transport of both Li ion and electrons. (ii) The presence of smaller surface pores in the dual pore-size Cu scaffold creates a larger surface area and dramatically increases the contact area between the active material and current collector, and markedly diminishes the interfacial resistance. This is also reflected in the decreased charge transfer resistance shown in Fig. 3.22. (iii) Cu foam with interconnected pores can relieve stress caused by the large volume changes of coated $SnO_2$ during cycling.

To further elucidate the superior stabilizing effect of $SnO_2$@Cu scaffold compared to the $SnO_2$ NPs control, the cross-section of the $SnO_2$ coating was examined using FIB milling and EDX mapping analysis after 50 cycles at 1 C (Fig. 3.23). The top $SnO_2$ coating layer was significantly expanded to ~2 μm after 50 cycles compared to the initial top coating layer of 500 nm (Fig. 3.14b); an increase of at least 300 % in the coating thickness was observed. However, the interior $SnO_2$ coating maintained a similar thin layer as indicated by the arrow, demonstrating that the interior coating layer was preserved without being pulverized by the significant volume changes from repeated Li ion inser-

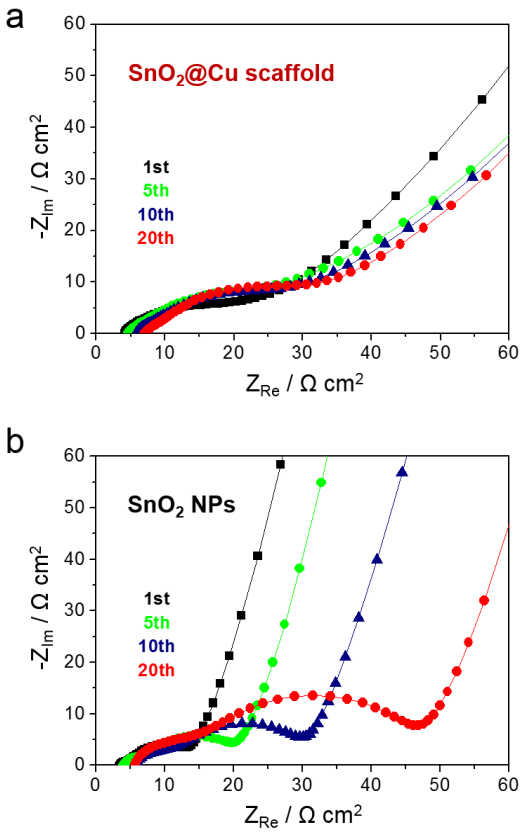


**Fig. 3.22** Cell impedance tests of (a) $SnO_2$@Cu foam and (b) $SnO_2$ NPs, after the 1st, 5th, 10th, and 20th cycles at 1 C.

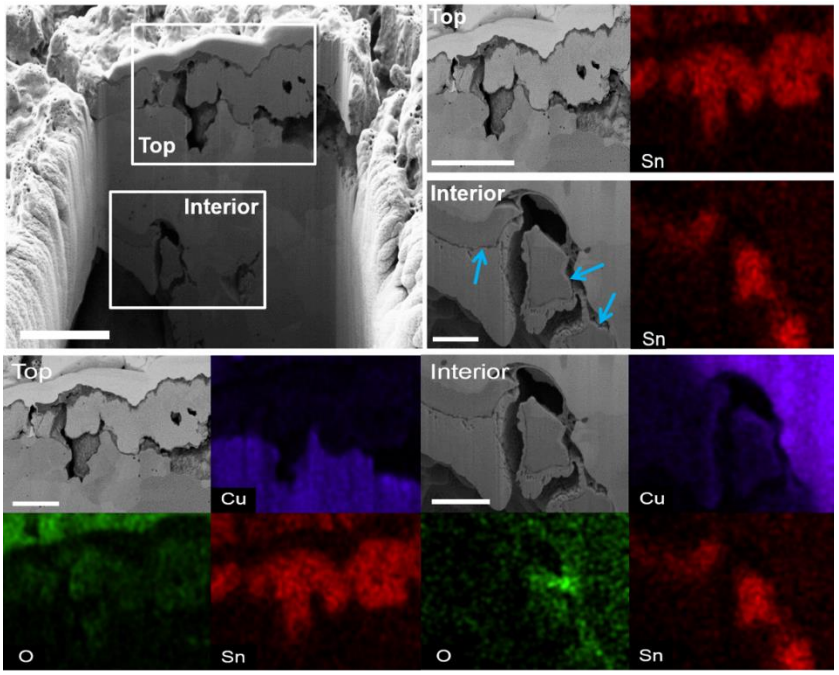


**Fig. 3.23** SEM and EDX images of cross-sections of top and interior regions of $SnO_2$@Cu scaffold after 50 cycles at 1 C after FIB milling with EDX map of Cu, Sn and O; scale bars, 2 μm and 1 μm.

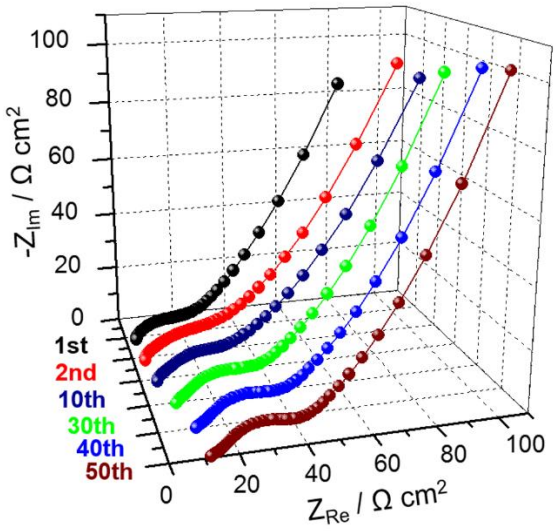


**Fig. 3.24** Cell impedance tests of $SnO_2$@Cu scaffold after selected cycles at 1 C.

tion and extraction. In addition, the electrochemical impedance spectroscopy (EIS) measurement of the $SnO_2$@Cu scaffold after completion of different cycles at 1 C was conducted (Fig. 3.24). There was no obvious increase in impedance after the 30th cycle, implying limited growth of the SEI layer, which is ascribed to the interior thin $SnO_2$ coating layer in the Cu scaffold; Moreover, a comparison of the EIS plots with $SnO_2$ NPs in Fig. 3.22 presents notably this feature.

### 3.3.4. Conclusions

A $SnO_2$-coated 3D porous Cu scaffold was developed by employing a novel combination of freeze-casting and sol-gel coating processes. The coated Cu scaffold with a 3D porous metallic network structure was fabricated and used in a lithium-ion battery anode for the first time. The unique 3D structure with a dual pore size and pore shape distribution enables fast transport of Li ion and electrons, and accommodates the large volume changes of the $SnO_2$ coating layer during cycling. As a result, the $SnO_2$-coated Cu scaffold exhibits enhanced Li ion storage capacity with cycling stability; more specifically, a high reversible capacity of 750 mAh $g^{-1}$ was achieved at 0.5 C, and, superior rate capabilities, close to the best performance of Sn-based nanoscale material so far, were achieved under various rate conditions. Most importantly, the foam fabrication by freeze-casting is versatile and can be used with other metals than Cu (e.g., Ni and Fe) and the foams can be extended to other high-capacity materials (e.g., Si and Ge) that currently experience cycling damage due to large volume changes with repeated Li ion insertion and extraction.

## 3.4. References


1. Bruce, P. G., Freunberger, S. A., Hardwick, L. J. & Tarascon, J.-M. Li-$O_2$ and Li-S batteries with high energy storage. *Nat. Mater.* **11**, 19–29 (2012).
2. Tarascon, J.-M. & Armand, M. Issues and challenges facing rechargeable lithium batteries. *Nature* **414**, 359–367 (2001).
3. Armand, M. & Tarascon, J. M. Building better batteries. *Nature* **451**, 602–607 (2008).
4. Arico, A. S., Bruce, P., Scrosati, B., Tarascon, J.-M. & Schalkwijk, W. V. Nanostructured materials for advanced energy conversion and storage devices. *Nat. Mater.* **4**, 366–377 (2005).
5. Deng, D., Kim, M. G., Lee, J. Y. & Cho, J. Green energy storage materials: Nanostructured $TiO_2$ and Sn-based annodes for lithium-ion batteries. *Energy Environ. Sci.* **2**, 818–837 (2009).
6. Chen, J. S. & Lou, X. W. $SnO_2$-Based Nanomaterials: Synthesis and Application in Lithium-Ion Batteries. *Small* **9**, 1877–1893 (2013).
7. Park, C.-M., Kim, J.-H., Kim, H. & Sohn, H.-J. Li-alloy based anode materials for Li secondary batteries. *Chem. Soc. Rev.* **39**, 3115–3141 (2011).
8. Wu, H. B., Chen, J. S., Hng, H. H. & Lou, X. W. Nanostructured metal oxide-based materials as advanced anodes for lithium-ion batteries. *Nanoscale* **4**, 2526–2542 (2012).

9. Lee, K. T. & Cho, J. Roles of nanosize in lithium reactive nanomaterials for lithium-ion batteries. *Nano Today* **6**, 28–41 (2011).

10. Cheng, Y.-T. & Verbrugge, M. W. The influence of surface mechanics on diffusion induced stresses within spherical nanoparticles. *J. Appl. Phys.* **104**, 083521 (2008).

11. Yuan, C., Wu, H. B., Xie, Y. & Lou, X. W. Mixed Transition-Metal Oxides: Design, Synthesis, and Energy-Related Applications. *Angew. Chem. Int. Ed.* **53**, 1488–1504 (2014).

12. Wang, C., Wu, H., Chen, Z, McDowell, M. T., Cui, Y. & Bao, Z. Self-healing chemistry enables the stable operation of silicon microparticle anodes for high-energy lithium-ion batteries. *Nature Chem.* **5**, 1042–1048 (2013).

13. Jiang, J. *et al*. Recent Advances in Metal Oxide-based Electrode Architecture Design for Electrochemical Energy Storage. *Adv. Mater.* **24**, 5166–5180 (2012).

14. Wang, B., Luo, B., Li, X. & Zhi, L. The dimensionality of Sn anodes in Li-ion batteries. *Materials Today* **15**, 544–552 (2012).

15. Zhang, H., Yu, X. & Braun, P. V. Three-dimensional bicontinuous ultrafast-charge and -discharge bulk battery electrodes. *Nat. Nanotechnol.* **6**, 277–281 (2011).

16. Vu, A., Qian, Y. & Stein, A. Porous Electrode Materials for Lithium-Ion Batteries-How to Prepare Them and What Makes Them Special. *Adv. Energy Mater.* **2**, 1056–1085 (2012).

17. Garcíaa, R. Ed. & Chiang, Y.-M. Spatially Resolved Modeling of Microstructurally

Complex Battery Architectures. *J. Electrochem. Soc.* **154**, A856–A864 (2007).

18. Zhang, H. & Braun, P. V. Three-Dimensional Metal Scaffold Supported Bicontinuous Silicon Battery Anodes. *Nano Lett.* **12**, 2778−2783 (2012).

19. Kim, J.-H., Myung, S.-T. & Sun, Y.-K. Molten salt synthesis of $LiNi_{0.5}Mn_{1.5}O_4$ spinel for 5 V class cathode material of Li-ion secondary battery. *Electrochim. Acta* **49**, 219–227 (2004).

20. Li, X., Dhanabalan, A., Gu, L. & Wang, C. Three-Dimensional Porous Core-Shell Sn@Carbon Composite Anodes for High-Performance Lithium-Ion Battery Applications. *Adv. Energy Mater.* **2**, 238–244 (2012).

21. Fu, Y. *et al.* Template-free synthesized Ni nanofoams as nanostructured current collectors for high-performance electrodes in lithium-ion batteries. *J. Mater. Chem. A* **1**, 10002–10007 (2013).

22. Li, C. C. *et al.* Compressed hydrogen gas-induced synthesis of Au–Pt core–shell nanoparticle chains towards high-performance catalysts for Li–$O_2$ batteries. *J. Mater. Chem. A* **2**, 10676–10681 (2014).

23. Takasaki, T. *et al.* Fiber-Type $Ni(OH)_2$ Electrode for Nickel-Metal Hydride Battery: Super High-Rate Charge/Discharge and Long Cycle-Life Performances. *J. Electrochem. Soc.* **159**, A1891–A1896 (2012).

24. Ni, W. *et al.* One-Pot Synthesis of Ultra-Light Nickel Nanofoams Composed of Nanowires and Their Transformation into Various Functional Nanofoams. *Small* **8**,

3432–3437 (2012).

25. Dutta, S., Bhaumik, A. & Wu, K. C.-W. Hierarchically porous carbon derived from polymers and biomass: effect of interconnected pores on energy applications. DOI: 10.1039/c4ee01075b.

26. Pikul, J. H., Zhang, H. G., Cho, J., Braun, P. V. & King, W. P. High-power lithium ion microbatteries from interdigitated three-dimensional bicontinuous nanoporous electrodes. *Nat. Commun.* **4**, 1732–1736 (2013).

27. Frackowiak, E. Carbon materials for supercapacitor application. *Phys. Chem. Chem. Phys.* **9**, 1774–1785 (2007).

28. Xia, K., Gao, Q., Jiang, J. & Hu, J. Hierarchical porous carbons with controlled micropores and mesopores for supercapacitor electrode materials. *Carbon* **46**, 1718–1726 (2008).

29. Liu, Z. *et al.* Sulfur–nitrogen co-doped three-dimensional carbon foams with hierarchical pore structures as efficient metal-free electrocatalysts for oxygen reduction reactions. *Nanoscale* **5**, 3283–3288 (2013).

30. Kim, O.-H. *et al.* Ordered macroporous platinum electrode and enhanced mass transfer in fuel cells using inverse opal structure. *Nat. Commun.* **4**, 2473–2481 (2013).

31. Srinivas, G., Krungleviciute, V., Guo, Z.-X. & Yildirim, T. Exceptional $CO_2$ capture in a hierarchically porous carbon with simultaneous high surface area and pore volume. *Energy Environ. Sci.* **7**, 335–342 (2014).

32. Qiu, H.-J., Ito, Y. & Chen, M. W. Hierarchical nanoporous nickel alloy as three-dimensional electrodes for high-efficiency energy storage. *Scripta Mater*. **89**, 69–72 (2014).

33. Deville, S. *et al*. Freezing as a Path to Build Complex Composites. *Science* **311**, 515–518 (2006).

34. Halloran, J. Making Better Ceramic Composites with Ice. *Science* **311**, 479–480 (2006).

35. Zhang, H. & Cooper, A. I. Aligned Porous Structures by Directional Freezing. *Adv. Mater.* **19**, 1529–1533 (2007).

36. Deville, S. Freeze-Casting of Porous Ceramics: A Review of Current Achievements and Issues. *Adv. Energy Mater.* **10**, 155–169 (2008).

37. Zhang, H. *et al*. Aligned two- and three-dimensional structures by directional freezing of polymers and nanoparticles. *Nature Mater.* **4**, 787–793 (2005).

38. Li, N., Martin, C. R. & Scrosati, B. A High-Rate, High-Capacity, Nanostructured Tin Oxide Electrode. *Electrochem. Solid-State Lett.* **3**, 316–318 (2000).

39. Li, N. & Martin, C. R. High-Capacity, Nanostructured Sn-Based Anode Prepared Using Sol-Gel Template Synthesis. *J. Electrochem. Soc.* **148**, A164–A170 (2001).

40. Schoof, H., Bruns, L., Apel, J., Heschel, I. & Rau, G. Einfluss des Einfriervorganges auf die Porenstruktur gefriergetrockneter Kollagenschwämme. *Ki—Luft und Kältetechnik* **34**, 247–252 (1998).

41. Chino, Y. & Dunand, D. C. Directionally freeze-cast titanium foam with aligned, elongated pores. *Acta Materialia* **56**, 105–113 (2008).

42. Ramos, A. I. C. & Dunand, D. C. Preparation and Characterization of Directionally Freeze-cast Copper Foams. *Metals* **2**, 260–273 (2012).

43. Sepulveda, R., Plunk, A. A. & Dunand, D. C. Microstructure of $Fe_2O_3$ scaffolds created by freeze-casting and sintering. submitted to *Materials Sci. and Eng. A.*

44. Fu, L.J. *et al.* Electrode materials for lithium secondary batteries prepared by sol–gel methods. *Progress in Materials Science* **50**, 881–928 (2005).

45. Chawla, S. K., Rickett, B. I., Sankarraman, N. & Payer, J. H. An X-ray Photo-Electron Sperctroscopic Investigation of the Air-formed Film on Copper. *Corrosion Science*, **33**, 1617–1631 (1992).

46. Iijima, J. *et al.* Native oxidation of ultra high purity Cu bulk and thin films. *Applied Surface Science* **253**, 2825–2829 (2006).

47. Ai, Z., Zhang, L., Lee, S. & Ho, W. Interfacial Hydrothermal Synthesis of $Cu@Cu_2O$ Core-Shell Microspheres with Enhanced Visible-Light-Driven Photocatalytic Activity. *J. Phys. Chem. C* **113**, 20896–20902 (2009).

48. Hua, Q., Chen, K., Chang, S., Ma, Y. & Huang, W. Crystal Plane-Dependent Compositional and Structural Evolution of Uniform $Cu_2O$ Nanocrystals in Aqueous Ammonia Solutions. *J. Phys. Chem. C* **115**, 20618–20627 (2011).

49. Poizot, P., Laruelle, S., Grugeon, S., Dupont, L. & Tarascon, J-M. Nano-

sizedtransition-metaloxidesas negative-electrode materials for lithium-ion batteries. *Nature* **407**, 496–499 (2000).

50. Hasan, M., Chowdhury, T. & Rohan, J. F. Nanotubes of Core/Shell Cu/$Cu_2O$ as Anode Materials for Li-Ion Rechargeable Batteries. *J. Electrochem. Soc.* **157**, A682–A688 (2010).

51. Courtney, I. A. & Dahn, J. R. Electrochemical and In Situ X-Ray Diffraction Studies of the Reaction of Uthium with Tin Oxide Composites. *J. Electrochem. Soc.* **144**, 2045–2051 (1997).

52. Li, J., Zhao, Y., Wang, N. & Guan, L. A high performance carrier for $SnO_2$ nanoparticles used in lithium ion battery. *Chem. Commun.* **47**, 5238–5240 (2011).

53. Srinivasan, N. R., Mitra, S. & Bandyopadhyaya, R. Improved electrochemical performance of $SnO_2$–mesoporous carbon hybrid as a negative electrode for lithium ion battery applications. *Phys. Chem. Chem. Phys.* **16**, 6630–6640 (2014).

54. Kravchyk, K *et al.* Monodisperse and Inorganically Capped Sn and Sn/$SnO_2$ Nanocrystals for High-Performance Li-Ion Battery Anodes. *J. Am. Chem. Soc.* **135**, 4199−4202 (2013).

55. Qin, J. *et al.* Graphene Networks Anchored with Sn@Graphene as Lithium-ion Battery Anode. *ACS Nano* **8**, 1728–1738 (2014).

56. Luo, B. *et al.* Reduced Graphene Oxide-Mediated Growth of Uniform Tin-Core/Carbon-Sheath Coaxial Nanocables with Enhanced Lithium Ion Storage

Properties. *Adv. Mater.* **24**, 1405–1409 (2012).

57. Luo, B. *et al.* Graphene-Confined Sn Nanosheets with Enhanced Lithium Storage Capability. *Adv. Mater.* **24**, 3538–3543 (2012).

58. Yu, Y *et al*. Li Storage in 3D Nanoporous Au-Supported Nanocrystalline Tin. *Adv. Mater.* **23**, 2443–2447 (2011).

59. Hou, X. *et al.* In Situ Deposition of Hierarchical Architecture Assembly from Sn-Filled CNTs for Lithium-Ion Batteries. *ACS Appl. Mater. Interfaces* **5**, 6672−6677 (2013).

60. Liao, J.-Y. & Manthiram, A. Mesoporous $TiO_2$-Sn/C Core-Shell Nanowire Arrays as High-Performance 3D Anodes for Li-Ion Batteries. *Adv. Energy Mater.* 1400403 (2014).

61. Chen, X. *et al.* 3D tin anodes prepared by electrodeposition on a virus scaffold. *J. Power Sources* **211**, 129–132 (2012).

62. Wang, C *et al*. Three-dimensional Sn-graphene anode for high-performance lithium-ion batteries. *Nanoscale* **5**, 10599–10604 (2013).

63. Han, S., Jang, B., Kim, T., Oh, S. M. & Hyeon, T. Simple Synthesis of Hollow Tin Dioxide Microspheres and Their Application to Lithium-Ion Battery Anodes. *Adv. Funct. Mater.* **15**, 1845–1850 (2005).

64. Lou, X. W., Chen, J. S., Chen, P. & Archer L. A. One-Pot Synthesis of Carbon-Coated $SnO_2$ Nanocolloids with Improved Reversible Lithium Storage Properties. *Chem.*

*Mater.* **21**, 2868–2874 (2009).

65. Han, F., Li, W.-C., Li, M.-R. & Lu, A.-H. Fabrication of superior-performance $SnO_2$@C composites for lithium-ion anodes using tubular mesoporous carbon with thin carbon walls and high pore volume. *J. Mater. Chem.* **22**, 9645–9601 (2012).

# 국문초록

청정에너지 시대의 도래와 더불어 전기자동차의 개발이 촉진되었고, 리튬 이온 전지를 이용한 하이브리드 자동차(HEVs, hybrid electric vehicles)가 상용화되었으며 이후 배터리 동력만으로 주행할 수 있는 순수 전기자동차(BEVs, battery electric vehicles)에까지 빠른 속도로 개발되고 있다. 전기자동차에서 배터리는 휴대전화 및 노트북 컴퓨터와 같은 소형 전자기기보다 50배 이상의 고출력이 요구되며, 이러한 고출력 특성은 전극 소재, 전극 구조, 전해질의 이온전도도 등 다양한 요인들과 관련되어 있다. 현재까지 알려진 음극 소재는 에너지(watt-hours)와 파워(watt) 특성이 상충관계(trade-off relation)를 이루고 있기 때문에, 고용량 소재의 고출력 특성 발현을 위한 연구들로 (1)새로운 소재의 개발 (2)전극의 박막화 (3)일체형 전극(integrated electrode)의 디자인 (4)제1원리 계산법(ab initio quantum chemistry methods)으로부터의 반응 메커니즘 이해 및 이를 통한 새로운 전극 소재로의 디자인으로 이루어져 오고 있다. 본 연구에서는 소재의 디자인과 일체형 전극 구조 및 박막화 특성을 통한 고출력화에 대해서 고려해 본다.

1장에서는 리튬 이온 전지에 대하여 간단히 소개하고, 양극과 음극 소재들을 각각 구조별과 반응 메커니즘별로 분류하여 살펴본다. 전형적인

고출력 특성의 음극 물질로 알려진 이산화티타늄과 고용량 음극 물질인 이산화주석에 대한 소개도 다룬다.

2장에서는 이산화티타늄의 전기화학적 특성에 대해서 다룬다. 특히 3가지 종류의 입자(particle) 크기 조절을 통해 이것이 출력 특성에 미치는 효과에 대해서 살펴본다. 구조적 변화를 *in-situ* synchrotron X선 회절(X-ray diffraction)을 통하여 분석하였다. 사이클이 진행됨에 따라 용량이 증가하는 활성화(activation)가 관찰되었으며, 이러한 현상은 삽입과 탈리의 반응 반응메커니즘을 따르는 구조적으로 안정한 음극 물질인 이산화티타늄에서 드물게 보고되는 경우이다. 이러한 현상의 원인으로 *in-situ* synchrotron X선 회절 분석에 의해 입자를 이루고 있는 격자(lattice) 팽창에 의한 활물질과 전해액의 접촉 면적 증가와 연관시켜 본다.

3장에서는 이산화주석의 전기화학적 성능을 향상시키기 위한 방법을 소개한다. 전형적인 배터리 전극이 2차원의(2D, 2-dimensional) 합판(laminate) 구조인 것과 비교하여, 3차원의(3D, 3-dimensional) 구리 폼(foam)을 전극에 적용하여 이산화주석의 증착을 위한 형판(template)으로 도입하였다. 집전체(current collector)와 이산화주석의 얇은 층 형성에 형판 역할을 하는 구리 폼은 빈 공간(void space)을 제공함으로써 이산화주석의 큰 부피팽창을 완화시키는 장점을 갖는다. 바인더와 도전재와 같은 첨가제를 필요로 하지 않는 이러한 일체형 전극은 사이클 후에도 그 구조적 온전함을 유지함과 동시에 높은 용량과 속도 특성, 안정적인 사이클 수명을 보인다. 또 다른

전극 구조로서, 구리 다층 조립(layer-by-layer assembly) 구조체를 소개한다. 구리 층 표면에 발달된 기공(pore)들은 하나의 층을 관통하고, 개방형(open) 기공 구조를 갖게 하는데, 이러한 높은 비표면적을 갖는 구리 다층 조립 구조는 고용량 물질인 이산화주석의 우수한 고출력 특성의 발현을 가능하게 한다.

**주요어: 리튬 이온 전지, 전극 구조, 고출력 밀도, 이산화티타늄, 이산화주석**

**학 번:** 2011-30279